

June 2017

Defects and Rearrangements in Disordered Solids

Sven Wijtmans
Syracuse University

Follow this and additional works at: <https://surface.syr.edu/etd>



Part of the [Physical Sciences and Mathematics Commons](#)

Recommended Citation

Wijtmans, Sven, "Defects and Rearrangements in Disordered Solids" (2017). *Dissertations - ALL*. 733.
<https://surface.syr.edu/etd/733>

This Dissertation is brought to you for free and open access by the SURFACE at SURFACE. It has been accepted for inclusion in Dissertations - ALL by an authorized administrator of SURFACE. For more information, please contact surface@syr.edu.

Abstract

In this thesis, I will investigate the properties of disordered materials under strain. Disordered materials encompass a large variety of materials, including glasses, polymers, granular matter, dense colloids, and gels. There is currently no constitutive equation based on microscopic observables that describes these materials. Given the prevalence and usefulness of these materials, we derive tools to aid our understanding of them. We develop a new method to isolate localized defects from extended vibrational modes in disordered solids. This method augments particle interactions with an artificial potential that acts as a high-pass filter: it preserves small-scale structures while pushing extended vibrational modes to higher frequencies. The low-frequency modes that remain are “bare” defects; they are exponentially localized without the quadrupolar tails associated with elastic interactions. We demonstrate that these localized excitations are excellent predictors of plastic rearrangements in the solid. We characterize several of the properties of these defects that appear in mesoscopic theories of plasticity, including their distribution of energy barriers, number density, and size, which is a first step in testing and revising continuum models for plasticity in disordered solids.

We additionally study the properties of rearrangement types in 2D disordered packings of particles with a harmonic potential at a range of packing fractions above jamming. We develop a generalizable procedure that classifies events by stress drop, energy drop, and reversibility under two protocols. Somewhat surprisingly, we find a large population of contact change events that have no associated stress drop. Reversible events become more common at high pressures above a packing fraction of $\phi = 0.865$, at which point line reversible events are more common than loop reversible events. At low pressures, irreversible events are associated with spatially extended events, while at high pressures reversible events are much more spatially localized.

Defects and Rearrangements in Disordered Solids

by

Sven Wijtmans

B.S., Harvey Mudd College, 2011

Dissertation

Submitted in partial fulfillment for the
degree of Doctor of Philosophy in Physics

Syracuse University

May 2017

Copyright ©Sven Wijtmans 2017

All Rights Reserved

Acknowledgements

I would like to express my most sincere gratitude to my advisor Lisa Manning for guiding me through my tumultuous journey through this process. I could not have done this without your patience and clarity of thought. I would like to thank my committee members Profs. Claudia Miller, Liviu Movileanu, Jennifer Schwarz, Joseph D Paulsen, and Alan Middleton. I would also like to thank Prof. Martin van Hecke and Merlijn van Deen from Leiden University, without whom Chapter 3 could not have been written, and all members of the Manning group, especially Max Bi, Matthias Merkel, and Peter Morse, for their advice. Finally, I am indebted to my family for supporting me during my years here, giving special thanks to my lovely wife for putting up with me this past year.

“The first duty of every [scientist] is to the truth, whether it’s scientific truth or historical truth or personal truth! It is the guiding principle on which science is based.”

Jean-Luc Picard, paraphrased

Contents

Abstract	i
Copyright	i
Acknowledgements	iv
List of Figures	viii
1 Introduction	1
1.1 Scope	1
1.2 Background	3
1.2.1 Amorphous Materials	3
1.2.2 Dynamical Matrix	3
1.2.3 Density of States	5
1.3 Continuum models	7
1.3.1 Shear transformation zones	7
1.3.2 Soft glassy rheology	8
1.3.3 Effective temperature	9
1.4 Rearrangements	10
1.4.1 T1 Transitions	11
1.4.2 Avalanches	12
1.4.3 Reversibility	12
1.5 Numerical model for simulations	13
1.5.1 Inter-particle Potentials	14
1.5.2 System preparation	15
1.5.3 Simulation steps	16
1.5.4 Conjugate Gradient Minimization	17
1.5.5 Fast inertial relaxation engine	17
1.6 Outline	18

2	Disentangling defects and sound modes in disordered solids	20
2.1	Introduction	20
2.2	Simulation Model	22
2.3	Results	25
2.3.1	Size and number density	27
2.3.2	Direction information and energy barriers	30
2.4	Discussion and Conclusions	33
2.5	Appendix A	34
2.6	Appendix B	38
2.7	Appendix C	39
2.8	Appendix D: Defect size and predictive capability	40
3	Distinguishing rearrangement events in disordered solids as a function of pressure	44
3.1	Introduction	44
3.2	Methods	47
3.3	Contact changes	48
3.4	Stress relaxation	48
3.5	Strain reversibility	50
3.6	Event size	54
3.7	Conclusion and outlook	54
4	Conclusion	57
4.1	Summary	57
4.2	Outlook	58
	Bibliography	60

List of Figures

1.1	Glasses and granular packings are both members of the same class of disordered or amorphous materials. [1]	4
1.2	Snapshot taken from a jammed packing at a packing fraction of $\phi = 0.9$. Particle radii ratio is 1.4(red):1(blue).	4
1.3	Density of states for a 3D system of harmonic spheres at various packings fractions $\delta\phi = \phi_c - \phi$. [2]	6
1.4	A typical low-frequency quasilocalized standard mode for a disordered 2D packing.	6
1.5	Typical stress-strain curve for a jammed packing undergoing simple shear. There are stress drops only at large scale particle rearrangements-plastic events, which can be reversible.	11
1.6	A T1 transition. Particles 1 and 4 are initially in contact, and particles 2 and 3 are not. After the transition, particles 2 and 3 are in contact, and particle 1 and 4 are not.	12
1.7	a) Line reversible event. b) Loop reversible event. c) irreversible event. d), e), and f) are equivalent to a),b),and c) with the affine portion subtracted off. Green pluses, blue circles, and red crosses mark the beginning, middle, and end of the particle tracks respectively, and particle outlines correspond to the beginning of the cycle. g) Below jamming reversibility phase diagram, showing line reversibility as black circles, loop reversibility as green triangles, and irreversibility as red squares. [3]	13
1.8	The Lees-Edwards boundary condition can be represented as offset cells, where simple strain is set by the offset and the box size.	14
1.9	Correlation lengths from left to right are 50, 20, 5, and 1. Particles are colored by the bond orientational order.	16
2.1	(a) A square grid of points is connected by a spring-like interaction. Movement of a grid point is defined by the weighted particle displacements. (b) A typical hybridized vibrational mode from a standard dynamical matrix. (c) A typical localized mode from an augmented dynamical matrix. (d,e) The sum of the magnitudes of particle displacements in the 30 standard (d) and augmented (e) modes with the lowest frequencies. The colorbar represents the magnitude of the summed polarization vector.	24

2.2	Energy due to augmentation, $\tilde{U} - U$, of a plane wave of wavenumber k for various number of grid points spacing a ranging from $L/2$ to $L/10$ at $L = 46$. The solid line corresponds to $a = L/7$. Results are shown both for the analytic prediction, as lines, and numerical results, as points, which do not differ significantly.	25
2.3	a) The radius of gyration of the 20 lowest frequency modes in 100 realizations are much smaller for augmented modes (solid line) than for standard modes (dashed line). b) Density of states plotted as number of modes per packing, for augmented (solid) and standard(dashed) modes. Localized modes (red) only appear in the augmented DOS, while the plane waves (blue) in the augmented system have increased energy.	26
2.4	a) The number of modes with $R_G < 16$ in the augmented system. The line is a Gaussian fit with $\mu = 6.79$ and $\sigma = 2.45$. b) The length scale extracted from an exponential fit to the radially averages distribution of displacement vectors for augmented localized modes. The line is a Gaussian fit with $\mu = 7.89$ and $\sigma = 2.01$	28
2.5	A soft cluster compared to the most similar augmented mode, of $R_G = 15.3$. The localization length of the augmented mode ($l_{mode} = 8.8$) is represented as a circle. (inset) Blue points are the radially averaged magnitudes of particle displacements $ \mathbf{e}_i $ a distances r from largest particle displacement; the red line is the best exponential fit.	29
2.6	a) Correlation function C_{SR} between soft spots and rearrangements generated from the localized augmented modes (magenta) are very similar to those for standard modes (black), and more accurate far from the event. Events are binned as a function of the strain required to get to the next particle rearrangement $(\gamma_c - \gamma)$. b) Comparison of the highest dot product between localized ($R_G < 16$) augmented modes (magenta) and standard modes (black). The various curves represent different distances in strain from the rearrangement. The solid lines correspond to strains close to a rearrangement $((\gamma - \gamma_c) < 10^{-4.5})$, the dashed lines are $10^{-4.5} \leq (\gamma - \gamma_c) \leq 10^{-3.5}$, and the dotted line represents $(\gamma - \gamma_c) \geq 10^{-3.5}$. The pdf was created from a cumulative distribution function using a Gaussian smoothing filter of $\sigma = .07$. We see that the localized augmented modes tend to match the rearrangement much better than the standard mode, especially far from the rearrangement as demonstrated by the magenta curves having larger weights near unity.	31
2.7	Probability distribution of energy barrier for standard (dashed), and augmented (solid) modes, collected over the 50 lowest frequency modes in 100 realizations are plotted separated by mode type as in Fig. 2.3. Localized augmented modes are more likely to have very low energy barriers. Curves were produced by smoothing the cumulative distribution function with a Gaussian filter of width 0.7.	32
2.8	Ratio of height variation Δh to mean height \bar{h} of a grid of gaussians of width σ and spacing a between each peak.	35

2.9	The 50 lowest frequency modes in 100 packings, sorted by type as in Fig.2.3b, plotted as a function of K . There are three regions: $0 < K < 0.01$, where the augmentation begins to have an effect, $0.01 < K < 0.02$, where the augmentation begins to greatly alter the mode structure, and $0.02 < K$, where the number of spurious localized modes grow linearly with K , as shown in the inset over a wider range of K	39
2.10	Ratio of energy barriers $\Delta U/\Delta U^{C2N}$ calculated using different definitions for what constitutes a particle rearrangement, as described in the main text. Box and whiskers contains 50 % and 92 % of the data points, respectively, blue bars denote the median, and outliers are circles.	40
2.11	Comparison of the separation distances between the center of a mode and the center of a rearrangement. We compare standard modes, augmented modes, and soft spots, near and far from the rearrangement, as well as a comparison to a random distribution of the same number as described in Appendix C. Each line is scaled by the expected value of a random distribution of the same number of candidates.	42
2.12	a) The number of clusters for the standard soft spots algorithm (black), as well as when using only the localized augmented modes ($R_G < 16$), with $N_p = 25$ (magenta) and $N_p = 40$ (red). Using only the localized modes gives fewer spots. Dashed lines are Gaussian fits. b) The average number of particles per soft spot. Colors are same as in a).	43
3.1	a) A 2D histogram of the stress drop/initial stress vs the rsq displacement of the particles during an event. There are two clear lobes: the upper right corresponds to a physical event. b) A 2D histogram of the stress drop/initial stress vs the energy drop/initial energy during an event. There are two clear lobes: the upper right corresponds to a physical event. c) A 2D histogram of the energy drop/initial energy vs the rsq displacement of the particles during an event. There are two clear lobes: the upper right corresponds to a physical event. The colorbar represents log number of events in each bin. All events that result in a new relaxed state occur in the white boxes.	46
3.2	The fraction of rearrangements that relax to the same (red) or different (blue) state under minimization at zero stress as a function of pressure for a 128 particle system.	49
3.3	Step 1: complete a forwards strain sweep, and identify rearrangement events. Step 2: Load in packing from after event at γ_1 , and strain till before γ_3 . Step 3: Strain backwards to the original leading strain.	50

3.4	a) Every rearrangement event binned as a function of the return distance Δr and max loop distance M , as described in the main text. Three clear regimes separate the events into irreversible (upper right), loop reversible (upper left) and line reversible (lower left). b) Every network event binned as a function of the return distance Δr and max loop distance M , as described in the main text. Three clear regimes separate the events into irreversible (upper right), loop reversible (upper left) and line reversible (lower left).	51
3.5	a) The fraction of irreversible rearrangement(+), line reversible rearrangement (o) loop reversible rearrangement (x), irreversible network (Δ) and reversible network (∇) events to total rearrangement events as a function of pressure. Error bars are smaller than symbols. b) The fraction of irreversible(+), line reversible(o) and loop reversible (x) events to total rearrangement events as a function of pressure. Error bars are smaller than symbols.	52
3.6	The size of an event is calculated by using the radius of gyration around the center of mass, where the magnitude of the particle displacement is used for mass in both equations.	54
3.7	Histogram illustrating frequency of stress drops as a function of pressure. The red line is the best separating plane between network events and rearrangements with $S \approx 10^{-5}P$.	56

For my family.

Chapter 1

Introduction

1.1 Scope

Many disordered systems, including granular systems, atomic and molecular glasses [4–6], foams, emulsions, pastes [7], and even granular fault gouges in earthquake physics [8] flow via local structural rearrangement. While the detailed interactions in these systems differ, the fact that they all flow via localized rearrangements gives hope that a universal description exists. In disordered solids such as granular materials, foams, and dense colloids, the mechanisms for flow and failure vary widely as a function of material preparation and the type of applied stress and remain poorly understood. On the macroscopic scale, solids can weaken via a reduced elastic modulus [9] or fail via localized rearrangements [10], sporadic large-scale avalanches [11–13], or continuously evolving extended shear bands [14–17].

The response of disordered solids to applied shear is similar to and different than deformation in crystals. In crystals, applying strain builds up stress, which is at first accommodated globally by a small, affine elastic change in the particle positions. As strain continues to build, some particles will move past each other, in a rearrangement. These rearrangements occur at lattice defects, which are the dislocations [18], easily identified by looking at the bond-orientational order. Once enough stress has built up, a rearrangement happens at a dislocation. Often whole rows of particles will participate in these

slip events. In fact, the types of rearrangements in crystals are well enumerated and well studied.

In disordered solids, such as granular materials [8, 19–21] and bulk metallic glasses [4–6], the initial story is the same—applying strain builds up stress, which is at first accommodated globally by a small, affine elastic change in the particle positions. Once enough stress has built up, it will be released in an event where several particles have large non-affine displacements [6, 22]. Generally, a particle will slip past other particles and acquire new neighbors. The simplest such event is a T1 transition, which involves 4 particles—larger and more complex rearrangements also occur. As there are no dislocations, identifying where this will occur a priori is difficult. In addition, the relationship between slip events is more complicated. Instead of an easily identified dislocation glide or climb, the effect of an initial particle slip event travels through the bulk of the material and may trigger other such events in what is called an avalanche.

Localized defects can self-organize, changing the bulk properties of materials. For example, shear bands, which are regions that flow faster than the rest of the material, are thought to develop when defects co-localize [15, 17]. In other regimes, self-organization of defects leads to avalanching, where a material deforms elastically until a stress-lowering rearrangement at one defect triggers a cascade of rearrangements at other defects [12]. Interesting memory effects [7, 23] may also be generated by self-organization of defects.

Defects play an important role in several mesoscopic phenomenological theories of plasticity, such as the theory of shear transformation zones (STZ) [22, 24], which given a population and energy scale for defects, predicts how the solid will fail, and the theory of soft glassy rheology (SGR) [25], which assumes a population of yielding mesoscopic regions.

To make predictions about such large-scale failure mechanisms, many continuum models [22, 26–29] make assumptions about the statistics of a solid’s complex potential energy landscape and how applied shear stress drives the system to explore mechanically stable minima within that landscape.

In addition, recent experiments and simulations suggest that particle rearrangements in periodically strained disordered solids can encode memories that can be read out using a proper strain protocol [23, 30]. Interestingly, several details of these memories (including

their robustness to noise) appear to depend on the interaction potential and corresponding properties of the potential energy landscape. Furthermore, the ability to encode memories has been tightly linked with the reversibility of rearrangement events.

For these reasons, it is critically important to characterize the elementary particle rearrangements that allow a solid to explore different mechanically stable states. However, there is no universally-accepted definition of when a particle packing has crossed to a “different state”.

While harder to identify than crystal dislocations, evidence is building that ‘soft spots’, where the rearrangements are more likely to occur, do exist. As discussed in the Introduction to Chapter 2, several methods have been developed that show a correlation between localized structural weak spots and rearrangements, though all have drawbacks. If we can better understand these soft spots, we will have taken a large step understanding the properties and deformation of disordered materials.

1.2 Background

1.2.1 Amorphous Materials

By now, it is well known that glasses and granular packings are members of the same class of materials and belong on the same phase diagram as shown in Fig. 1.1, first proposed by Liu and Nagel in 1998[1] and studied by many others [31–34].

My work studies athermal packings of particles with only repulsive interactions, such that I am studying packings along the $1/\text{density}$ axis of Fig. 1.1. As a system of equally sized particles will form a crystal under pressure, I use the Kob-Anderson model [35], which consists of two sizes of particles such that no crystal forms, as seen in Fig. 1.2.

1.2.2 Dynamical Matrix

We can calculate the linear response of the packing by calculating the eigenvectors and eigenvalues of the Hessian matrix, which is defined by the following equation:

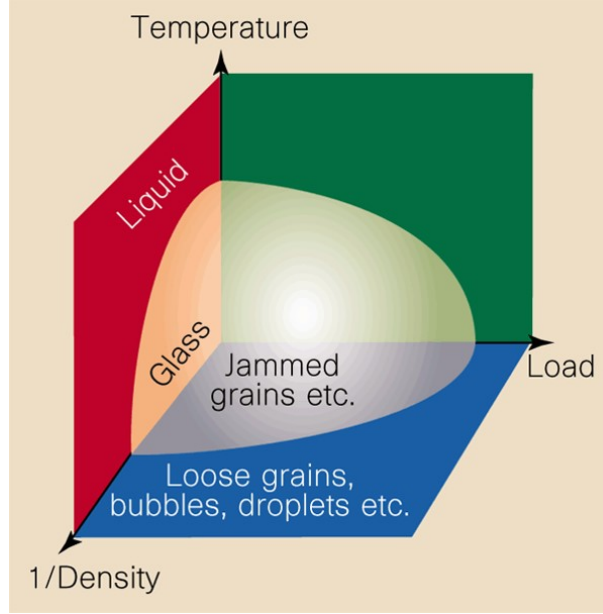


FIGURE 1.1: Glasses and granular packings are both members of the same class of disordered or amorphous materials. [1]

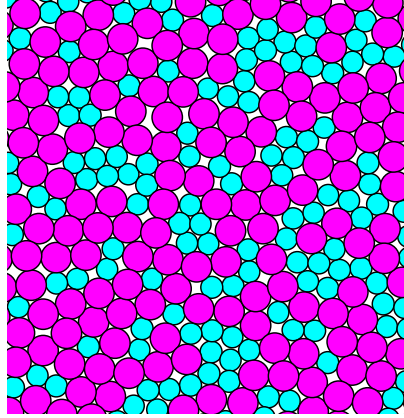


FIGURE 1.2: Snapshot taken from a jammed packing at a packing fraction of $\phi = 0.9$. Particle radii ratio is 1.4(red):1(blue).

$$H_{i\alpha j\beta} = \frac{\partial^2 U}{\partial u_{i\alpha} \partial u_{j\beta}}, \quad (1.1)$$

where U is the total energy of the system and u are particle displacements. For simple two-body potentials, it can be shown that the Hessian can be written in terms of inter-particle energies [11], rather than the total energy, in the following form:

$$H_{i\alpha j\beta} = \begin{cases} \frac{\partial^2 V_{ij}}{\partial r_\alpha \partial r_\beta}, & \text{off diagonal} \\ -\sum_{i \neq j} H_{i\alpha j\beta}, & \text{on diagonal .} \end{cases} \quad (1.2)$$

The rows of the matrix therefore sum to zero, which is necessary for force balance in the packing. The related dynamical matrix \mathcal{M} is simply the Hessian Matrix, with scaling by the particle masses.

$$\mathcal{M} = MH, \quad (1.3)$$

where $M_{ij} = m_i \delta_{ij}$ and m_i is the mass of particle i . In the simulations described here, $m_i = 1$ for all i , so $\mathcal{M} = H$, to be consistent with previous literature [36–38] .

The total energy of the packing is the sum of the interparticle energies

$$U = \sum_{ij} V_{ij}. \quad (1.4)$$

The change in energy ΔU generated by displacing all the particles along some direction u is

$$\Delta U = \frac{1}{2} H_{ij\alpha\beta} u_{i\alpha} u_{j\beta}. \quad (1.5)$$

The normal modes are the eigenvectors of the dynamical matrix, and their associated eigenvalues are the frequencies.

While in simulation the dynamical matrix, and thus the vibrational modes, are easy to calculate, in experiments it is more difficult. It is possible to extract the vibrational modes from experiments, by characterizing time averaging two-particle correlation functions [39].

1.2.3 Density of States

The energy spectrum of a disordered packing is well known. All disorders solid have a typical density of states—the distribution of the energies of the modes. At low frequencies, the density follows the Debye prediction and goes proportional to $\sim \omega^{d-1}$, as modes are plane-wave-like. At medium frequencies, the density of states rises above the Debye prediction, in what is known as the Boson Peak. This peak occurs at a characteristic length scale ω^* , above which modes no longer have plane-wave-like nature [2]. At high

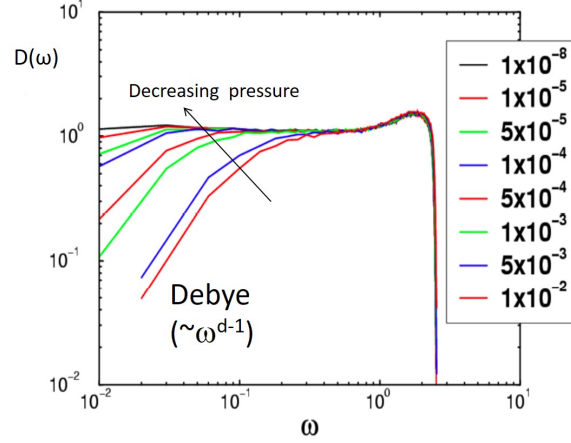


FIGURE 1.3: Density of states for a 3D system of harmonic spheres at various packings fractions $\delta\phi = \phi_c - \phi$. [2]

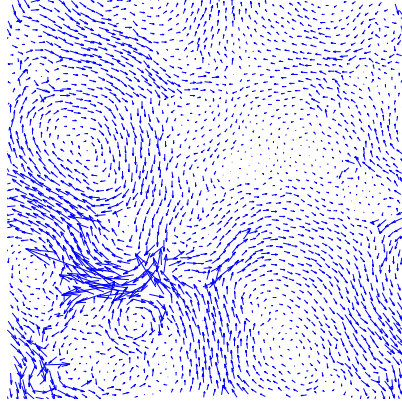


FIGURE 1.4: A typical low-frequency quasilocalized standard mode for a disordered 2D packing.

frequencies, the density falls off and goes to zero. This behavior can be seen in Fig. 1.3 for systems at several packing fractions.

Phonon-like modes and defect-localized modes both have low frequencies and exist below the boson peak. In disordered packings, it has been observed that phonon-like-modes are roughly at the same energy as localized modes. According to perturbation theory, we expect that modes with similar energies will mix and generate hybridized low-frequency modes— mixtures of phonon-like-modes and local modes. Such a mode is seen in Fig. 1.4.

1.3 Continuum models

One goal of this work is to constrain continuum models for amorphous plasticity that postulate the existence of soft regions. Therefore we briefly describe two of the most popular such models, shear transformation zone (STZ) and soft glassy rheology (SGR).

1.3.1 Shear transformation zones

Shear transformation zone theory assumes some population of shear transformation zones (STZs). They have an orientation and can be ‘activated’- they deform in response to stress. The number density and internal degrees of the STZs then inform how the packing evolves. These internal degrees of freedom include the orientation and the activation energy—the energy barrier. The STZs do not only interact with the environment, but also with each other. STZs have a formation energy related to the effective disorder temperature. The full STZ equations for an athermal amorphous solid [15, 22, 24, 40–42] are

$$\tau_0 D_{ij}^{pl}(s, \chi) = \frac{v_0}{V} (R(s)N_- - R(-s)N_+) = \epsilon_0 e^{-1/\chi} \frac{s_{ij}}{s} C(s) (T(s) - M(s)). \quad (1.6)$$

The plastic part of the rate of deformation tensor D_{ij}^{pl} depends on the rate R at which STZs ‘flip’, and the number N of positively and negatively oriented defects transitioning from one state to the other, controlled by the molecular timescale τ_0 such as the Debye frequency. v_0 is a characteristic strain associated with an STZ flip and V is a unit of volume. N is in turn written using a Boltzmann-like factor for the effective disorder temperature χ and factors that are derived from the STZs.

$$\tau_0 \dot{N}_{\pm} = R(\pm s)N_{\mp} - R(\mp s)N_{\pm} + \Gamma(s) \left(\frac{N_{eq}}{2} - N_{\pm} \right). \quad (1.7)$$

The number of defects is governed by the rate at which they flip, and also the creation and annihilation rate Γ of new STZs due to noise, modulated by the equilibrium number of STZs.

$$R(s) = R_0(s) \exp\left(-\frac{\Delta(s)}{\theta}\right); \Delta(s) = \Delta_0 e^{-s/\bar{\mu}}. \quad (1.8)$$

The transition rate between defects is exponential in the energy barriers $\Delta(s)$ between the states. The energy barriers are drawn from an exponential distribution.

The creation-annihilation term Γ is the most complex:

$$\Gamma(s) = \frac{2C(s)(\mathcal{T}(s) - M(s))(s/s_0 - \xi(M))}{1 - M(s)\xi(M)}. \quad (1.9)$$

$$C(s) = \frac{1}{2}(R(s) + R(-s)), \quad (1.10)$$

$$\mathcal{T}(s) = \frac{R(s) - R(-s)}{R(s) + R(-s)}, \quad (1.11)$$

$$M(s) = \frac{s_0}{2s} \left(\left(1 + \frac{s_0}{s}\mathcal{T}(s)\right) - \sqrt{\left(\left(1 + \frac{s_0}{s}\mathcal{T}(s)\right)^2 - 4\frac{s}{s_0}\mathcal{T}(s)\right)} \right), \quad (1.12)$$

$$\xi(M) = \frac{1}{s_0}\mathcal{T}^{-1}(M), \quad (1.13)$$

such that $\mathcal{T}(s_0\xi(M)) = M$. In the end, there are several parameters: the effective disorder temperature χ , the energy barrier required to activate a defect Δ , the equilibrium number of defects N_{eq} . The disorder temperature can also evolve with time, and has its own set of equations describing this evolution. STZ theory has had excellent qualitative agreement with experiment[24, 41]. One drawback of STZ theory is that the microscopic parameters have historically been identified from fits to macroscopic data, as it has not been possible to identify STZs in experiment or simulations.

1.3.2 Soft glassy rheology

Soft glassy rheology [25, 26] assumes that the solid is composed a number of mesoscopic regions, each with a stress threshold taken from a distribution. Each region has a separate have a max yield drawn from an exponential distribution. This is an extension of the Bouchard Trap model[43], in which an exponential distribution of barrier heights are activated thermally, leading to glassy behavior. SGR adds strain and replaces the thermal

temperature with an effective temperature χ due to mechanical noise generated by regions elsewhere in the system. The model assumes local linearity between stress and strain of the form $\sigma_{loc} = kl$, where k is an elastic constant. Each region has a probability P of being in a state with yield energy E , local strain l of

$$\frac{\partial}{\partial t}P(E, l, t) = -\dot{\gamma}\frac{\partial}{\partial l}P - \Gamma_0 e^{-(E-(1/2)kl^2)/\chi}P + \Gamma(t)\rho(E)\delta(l). \quad (1.14)$$

The evolution of each region is a combination of stress increase due to loading the packing at rate $\dot{\gamma}$, interaction-activated yielding with yielding rate Γ , and creations of new regions from the activated ones now with zero local stress and an yielding energy drawn from the exponential distribution $\rho(E) = \exp(-E)$.

$$\Gamma(t) = \Gamma_0 \left\langle e^{-(E-(1/2)kl^2)/\chi} \right\rangle_P = \Gamma_0 \int dE dl P(E, l, t) e^{-(E-(1/2)kl^2)/\chi}. \quad (1.15)$$

The total yielding rate $\Gamma(t)$ is the expectation value for the number of yielding sites. The macroscopic stress can be computed from the average local stresses

$$\sigma(t) = k \langle l \rangle_P \equiv k \int dE dl P(E, l, t) l. \quad (1.16)$$

The primary parameters in this model are the yield attempt frequency Γ_0 and the effective temperature χ . One drawback of SGR theory is that the evolution of the effective temperature cannot be derived from either first principles or mesoscopic principles [44]. Additionally, there exists experimental discrepancy with SGR predictions [45].

1.3.3 Effective temperature

Both of these models depend on an effective disorder temperature. It is common in continuum mechanics develop constitutive relations that depend on thermodynamic variables. However, the normal statistical physics temperature as measured by a thermometer is not usually relevant, as it has been shown [46–48] that athermal systems seem to obey a fluctuation-dissipation relation with a new, effective coefficient. In disordered system, there are two contributions to the entropy: the number of metastable states, called the configurational entropy, and the number of configurations within these metastable basins, called the vibrational energy [49]. In many cases, the effective temperature has

been linked to the configurational entropy. For powders and granular materials, Edwards [50] suggested that the free volume was the conjugate variable to the configurational entropy, and introduced a compactivity or angoricity. The compactivity takes the place of temperature, such that

$$\frac{1}{X} = \frac{\partial S(V)}{\partial V} \quad (1.17)$$

However, this formulation ignores the important contributions of force chains and local stresses. Therefore a generalized version of the Edward formulation [51] was developed. In this formulation, the conserved quantity is the force-moment tensor

$$\hat{\Sigma} = \sum_{m,n} d_{mn} f_{mn} \quad (1.18)$$

where d_{mn} is the vector pointing from the center of particle m to the interparticle contact with its neighbor particle n , f_{mn} is the interparticle contact force. The temperature-like variable is named the angoricity

$$\alpha_{\mu\lambda} \equiv \frac{\partial S(\hat{\Sigma})}{\partial \Sigma_{\mu\lambda}} \quad (1.19)$$

This is a likely candidate for the disorder temperature used in both the STZ and SGR paradigms, and has been shown to work in an SGR-like theory [52–55]. In STZ theory, it has been proposed[15] that the effective temperature sets the density of STZs:

$$\dot{\Lambda} = \Gamma(e^{-1/\chi} - \Lambda). \quad (1.20)$$

where Λ is the STZ density.

1.4 Rearrangements

In disordered materials, stress is not accommodated by continuous affine motion, but by sudden events where many particles move at once, termed plastic events. Depending on the system and the event, such an event could involve anywhere from four particles to the entire system.

Stress-strain curves such as the one in Fig 1.5 clearly show the sudden nature of these events, and demonstrate that particle motion is a combination of slow affine motion where

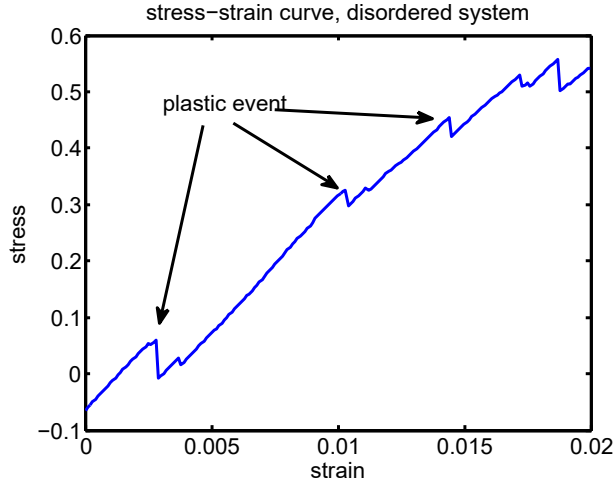


FIGURE 1.5: Typical stress-strain curve for a jammed packing undergoing simple shear. There are stress drops only at large scale particle rearrangements-plastic events, which can be reversible.

the stress accumulated, punctuated by plastic events that reduce the stress in the system. Note that the plastic events are of different sizes—and are distributed by the power law

$$\langle \delta\sigma \rangle \sim N^{-2/3} \quad (1.21)$$

as investigated by Dubey *et al.* [56].

1.4.1 T1 Transitions

The simplest common non-affine rearrangement that allows particles to move is called the T1 transition. A T1 transition involves four particles in contact with each other. Each touches its neighbors on the outside, but only one pair contacts across the center. A T1 transition is an event where this center pair changes, such that the other 2 particles are in contact across the center, as shown in Fig. 1.6. This transition is the most fundamental plastic rearrangement and involves several particles in close proximity changing the contact network.

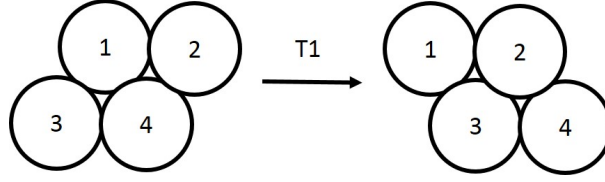


FIGURE 1.6: A T1 transition. Particles 1 and 4 are initially in contact, and particles 2 and 3 are not. After the transition, particles 2 and 3 are in contact, and particle 1 and 4 are not.

1.4.2 Avalanches

Often, one rearrangement event will trigger a large rearrangement that can span much of the system. These large bulk rearrangements are known as avalanches- the ordinary landslide from which this takes its name is, in fact, an example of an avalanche in a granular packing. The power law statistics for avalanches have been well studied [13, 57–60]. Avalanches are known to start at a defect but can grow to encompass the whole packing.

1.4.3 Reversibility

While reversing the strain cannot undo large events such as avalanches, smaller events can be reversible [61].

Below jamming, there is a clear separation between three types of reversible behavior. During a single shear cycle, Shreck *et al.* [3] classified the behavior of particles. At low strains and packing fractions, particles do not come into contact or deflect off each other, and thus have particle paths that reverse exactly. These we call line-reversible events. At higher strains and packing fractions, particles return to their previous positions but follow different paths back. These we call loop reversible. Just below jamming and at high packing fractions, they see irreversible events, where particles do not return to their original positions. These behaviors are shown in Fig. 1.7.

Above jamming, the situation appears more complicated, as reversible and irreversible T1 events exist at the same packing fraction and shear cycle [62]. To compensate, many have studied the proportion of irreversible events during shear cycles [7, 30, 63]. Interestingly, below some critical strain value, a cycled system will reach a reversible steady-state, while

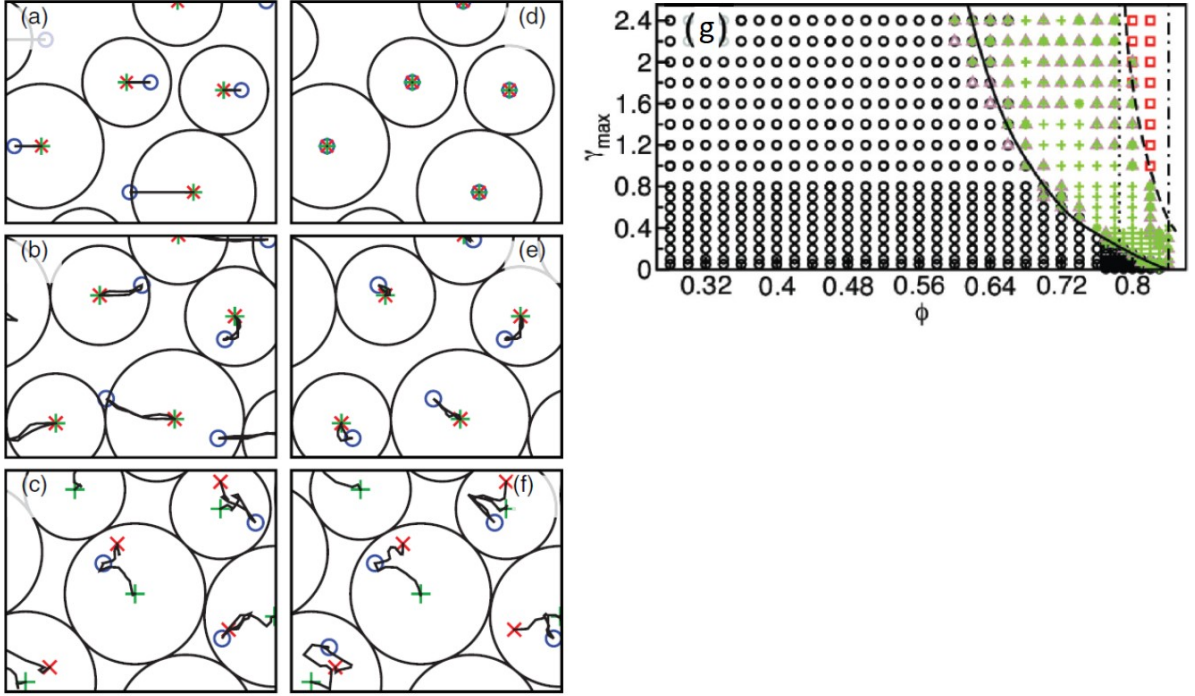


FIGURE 1.7: a) Line reversible event. b) Loop reversible event. c) irreversible event. d), e), and f) are equivalent to a), b), and c) with the affine portion subtracted off. Green pluses, blue circles, and red crosses mark the beginning, middle, and end of the particle tracks respectively, and particle outlines correspond to the beginning of the cycle. g) Below jamming reversibility phase diagram, showing line reversibility as black circles, loop reversibility as green triangles, and irreversibility as red squares. [3]

above it will remain irreversible [7]. This steady state can even hold memory, as a system cycled at one strain amplitude will see a signature at that amplitude if sheared further [30].

1.5 Numerical model for simulations

We study these phenomena in computer simulations, where the exact position and energy of every particle is known. There are many parameter choices and a variety of techniques for implementing dynamics in these systems.

The first choice is the number of dimensions. 1D has some applications [64], but most work focuses on common higher dimensions. 2D is physically realistic for a number of different systems. However, 2D simulations with particles of equal size will crystallize. Therefore

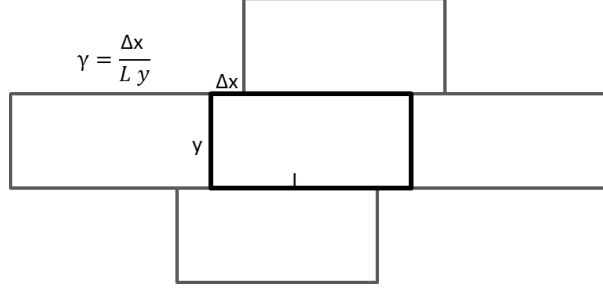


FIGURE 1.8: The Lees-Edwards boundary condition can be represented as offset cells, where simple strain is set by the offset and the box size.

in order to perform 2D simulations of disordered materials, it is required to have particles of different sizes [35]. 3D is, of course, the most realistic, but computation time scales with the box length cubed instead of box length squared and they are more difficult to visualize. Given that the number of particles per side in a simulation can typically be 50, 3D simulations can quickly become very expensive. Higher dimensions, while not physical, can be used to approximate mean field theories—in infinite dimensions, mean field assumptions become exact[65, 66].

It is well known that the size of a system can affect the results of a simulation [12, 67–69]. There is a tradeoff between accuracy of result and simulation time. In cases where we are interested in the thermodynamic limit, we will study different system sizes to understand finite-size effects.

One common boundary condition when working with sheared systems in the Lees-Edwards boundary condition, shown in Fig. 1.8. As in normal periodic boundary conditions, the right and left sides of the box are connected, as are the top and bottom. However, the image box on the top is offset by some amount—which becomes the shear strain on the system. This offset can be changed in order to shear the system. As the boundary moves, particles on one side of a boundary experience force from the ‘moving’ image particles on the other side of the boundary, creating shear.

1.5.1 Inter-particle Potentials

Particles in simulations often interact via a simple two-body interaction potential, which can be categorized a hard or soft. A hard sphere/disk potential (V_{hard}) is one where particles cannot overlap but are otherwise free to move. Such a potential cannot explore

conditions above jamming, as that would require particle overlap and thus an infinite system energy:

$$V_{hard} = \begin{cases} \infty & \delta > 0 \\ 0 & \delta \leq 0 \end{cases} \quad (1.22)$$

where δ is the particle overlap.

A soft sphere potential (V_{soft}) is short range potential in which it costs energy for particles to overlap, but there is no energy cost when the particles are not touching:

$$V_{soft} = \begin{cases} \kappa \delta^\alpha & \delta > 0 \\ 0 & \delta \leq 0 \end{cases} \quad (1.23)$$

where κ is a force constant and α is some power. $\alpha = 2$ is called a harmonic potential, as the interactions between particles are that of springs. $\alpha = \frac{5}{2}$ is the Hertzian potential which is the exact scaling potential of the overlap of elastic spheres as a function of the overlap between their centers—assuming the strains are small and within the elastic limit.

The Lennard-Jones potential is a long range potential that mimics certain features of atomic interaction potentials. Particles are repelled at close range, and attracted at long range, with a ‘well’ representing the lowest energy state at a ‘distance’ equal to the particle ‘radius’.

$$V_{LJ} = \epsilon \left(\left(\frac{\sigma}{r_m} \right)^{12} - \left(\frac{\sigma}{r_m} \right)^6 \right) \quad (1.24)$$

where ϵ is the depth of the energy well and r_m is the position of the well.

While these are the most common potentials used in these simulations, there are others used in more specialist applications. Additionally, many extra terms can be added to simulate other effects such as friction, wetting, or nonspherical particle shape.

1.5.2 System preparation

There are several ways of preparing random packings of particles. An infinite temperature quench is a protocol where all particles are placed randomly in the box at their full size. The energy is then minimized to reach a locally stable state. This corresponds to the (impossible) physical process of having the particles move in a gas at an infinite

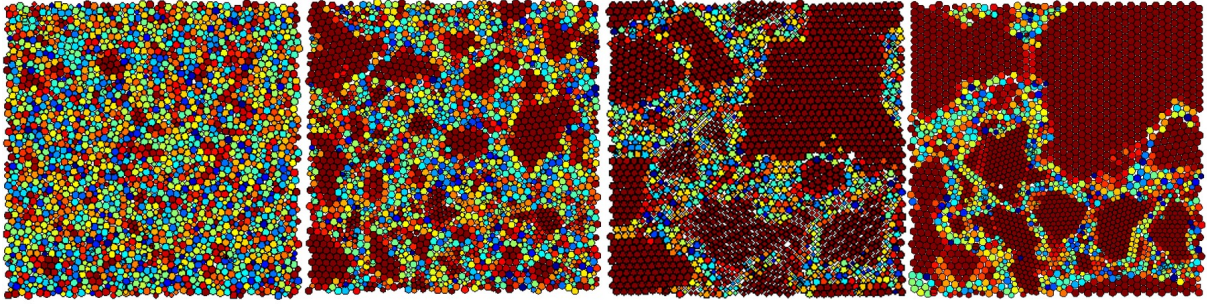


FIGURE 1.9: Correlation lengths from left to right are 50, 20, 5, and 1. Particles are colored by the bond orientational order.

temperature, and then instantly removing all the kinetic energy from the system. This is a relatively fast and inexpensive way to create a disordered packing.

The Lubachevsky-Stillinger algorithm is an algorithm in which particles are initially placed randomly as point particles (though it is possible to control the degree of disorder). The particles are slowly grown until the desired packing fraction is reached. This method has the benefit of being able to create packings with differing degrees of disorder. By weighing the radii of a particle by a Gaussian random distribution with a set correlation length, we can choose the degree of disorder in the packing, as seen in Fig. 1.9.

1.5.3 Simulation steps

There are several different protocols for shearing a simulated packing of particles that reflect the competing timescales in those systems. The main ones are the timescale for particles to relax to a local energy minimum and the timescale of strain.

Here we perform athermal quasistatic simulations (AQS), where the timescale of strain is taken to be infinitely large compared to the timescale of relaxation. In this protocol, the packing is sheared a small amount, whereupon the energy is minimized, and then sheared again. This ensured that the packing is always at an energy minimum.

To do this, an energy minimization algorithm must be used. While steepest descent is the simplest algorithm, it is also very slow, especially when far from the minimum, such as the start of the infinite quench. In these cases, a conjugate gradient algorithm is much more efficient. When the packing is close to the local minimum—such as when there has

been only a small step away, then a line search algorithm is faster than the conjugate gradient algorithm. A good compromise between speed and capturing realistic physics is the FIRE algorithm, which runs particle dynamics in between steps with a damping term.

How small do the steps need to be? As the packing undergoes long periods of smooth motion punctuated by bursts of motion at a rearrangement event, a single step size is not efficient. We use two different protocols. In one protocol, we do a universal sweep forwards with a single set large step size. This misses the dynamics of the plastic events but does locate them. In the second protocol, using a bisection algorithm, we then load the packing before the event and take smaller step sizes in order to locate the event more accurately. This is done several times until we have a set of very small strain steps across the event.

1.5.4 Conjugate Gradient Minimization

The conjugate gradient minimization method is a numerical method for solving large systems of linear equations, that is, systems of the form

$$A\vec{x} = \vec{b} \tag{1.25}$$

where A is a positive-definite matrix, \vec{x} is an unknown vector, and \vec{b} is a known vector.

Rather than following the gradient down to the minimum— a process known as steepest decent— the conjugate gradient method finds a spanning set of orthogonal vectors, takes a quadratic approximation in each direction, and jumps to the bottom of each, thus finding the minimum in N steps, where N is the full dimensionality of the problem. The vectors are found using Gram-Schmidt and the fact that the residual after a step will be orthogonal to all previous steps.

1.5.5 Fast inertial relaxation engine

The second protocol uses a bisection algorithm to identify and zoom in on plastic events. Large strain steps are taken forwards until an event is identified. A bisection algorithm

is then used to determine the exact location of the minimum. Once found to sufficient tolerance, the points searched by the bisection algorithm that occurs after the plastic event are ignored, and the process repeats for the next plastic event. The energy is minimized at each step by the (Fast inertial relaxation engine) FIRE algorithm with velocity-verlet MD step given below:

$$\vec{a}(t) = -\frac{1}{M}\vec{F}(t), \quad (1.26)$$

$$\vec{v}(t + \delta t) = \vec{v}(t) * c + \vec{a}(t)\delta t, \quad (1.27)$$

$$\vec{v}(t + \delta t) = (1 - \alpha)\vec{v}(t + \delta t) + \alpha \frac{\vec{F}(t)}{|\vec{F}(t)|} |\vec{v}(t + \delta t)|, \quad (1.28)$$

$$\vec{r}(t + \delta t) = -\vec{r}(t) + \vec{v}(t + \delta t)\delta t, \quad (1.29)$$

where $\vec{F} = \frac{\partial U(t)}{\partial \vec{r}}$, and initially $\alpha = \alpha_{start}$. If $\vec{v} \cdot \vec{F} > 0$ for several steps, α is slightly decreased, to indicate confidence in the direction of motion. If $\vec{v} \cdot \vec{F} \leq 0$, α is reset to the original α_{start} . This is repeated until the energy no longer changes from step to step below some tolerance.

1.6 Outline

The aim of this dissertation is to predict and characterize particle-scale rearrangements in disordered solids. We answer the questions: What are the fundamental units of plasticity? How can we predict where amorphous solids will deform? What does it mean for a system to be in a new state? What makes some rearrangements reversible and others non-reversible?

In Chapter 2, we develop a new method to isolate localized defects from extended vibrational modes in disordered solids. This method augments particle interactions with an artificial potential that acts as a high-pass filter: it preserves small-scale structures while pushing extended vibrational modes to higher frequencies. The low-frequency modes that remain are “bare” defects; they are exponentially localized without the quadrupolar tails associated with elastic interactions, and do an excellent job of predicting plastic rearrangements. We identify a robust definition for the energy barrier associated with each

defect, which is an important parameter in continuum models for plasticity. We find that the energy barriers for localized modes are less than the energy barriers for quasilocalized modes. We also quantify other important parameters for continuum models, including the size and number density of defects.

In Chapter 3 we study rearrangements in disordered packings of particles with a harmonic potential at a range of packing fractions above jamming. We develop a generalizable procedure that classifies events by stress drop, energy drop, and reversibility. We show that changes in the contact network are not sufficient to generate stress drops and that only about 10% of contact changes correspond to stress drops. Additionally, we probe the state of the packing by relaxing the boundary conditions, allowing the system to relax to a state of zero stress, and demonstrate that all contact changes that lack an associated stress drop relax to an identical zero-stress state. We also examine the reversibility of events by performing a single strain cycle around them. We characterize the frequencies and relationships between these different types of rearrangement events.

Finally, Chapter 4 discusses the significance of these results and highlights direction for future research.

Chapter 2

Disentangling defects and sound modes in disordered solids

2.1 Introduction

Under applied stress, solids can flow plastically. In crystals, this flow is controlled via rearrangements at lattice defects, which are the dislocations [18], easily identified by looking at the bond-orientational order. In disordered solids, such as granular materials [8, 19–21] and bulk metallic glasses [4–6] the structural defects are not easily identifiable using structural data, though the rearrangements are still localized [6, 22].

Localized defects can self-organize, changing the bulk properties of materials. For example, shear bands, which are regions that flow faster than the rest of the material, are thought to develop when defects co-localize [15, 17]. In other regimes, self-organization of defects leads to avalanching, where a material deforms elastically until a stress-lowering rearrangement at one defect triggers a cascade of rearrangements at other defects [12]. Interesting memory effects [7, 23] may also be generated by self-organization of defects.

Defects play an important role in several mesoscopic phenomenological theories of plasticity, such as the theory of shear transformation zones (STZ) [22, 24], which given a population and energy scale for defects, predicts how the solid will fail, and the theory of soft glassy rheology (SGR) [25], which assumes a population of yielding mesoscopic regions.

Isolating and quantifying features of defects in disordered solids has proved difficult. Finding the precise set of particle displacements that allow the system to rearrange at the lowest energy cost is computationally difficult. Observations that the low-frequency linear vibrational modes are strongly correlated with particle rearrangements and plasticity [70, 71] suggest that low-frequency localized excitations have very low energy barriers and therefore may identify defects. However, this conjecture is difficult to test because individual low-frequency normal modes are quasi-localized with long-ranged quadrupolar tails required to satisfy long-range elasticity.

One approach to overcoming this difficulty is to identify localized regions with the largest displacements in the lowest frequency modes. One finds that they do cluster into soft spots that identify locations where rearrangements are likely to occur [10]. This method has been extended to glasses at various temperatures [72], in different geometries [38], and to identify the approximate directions of particle displacements [73]. Building on these observations, a new machine learning method has been developed to identify softness fields in disordered solids [74]. A related approach characterizes the nonlinear response and uses an iterative approach to identify soft nonlinear modes and their associated energy barriers [75].

A different, yet complementary approach analyzes the response of circular regions of particles to applied shear in many directions [76], and also finds evidence for pre-existing structural defects. This method effectively predicts rearrangement sites, orientations, and energy barriers.

However, there are drawbacks to each of these approaches. The soft spots algorithm contains systematic errors due to hybridization of soft spots and sound modes [10], while the machine learning algorithm does not identify directions of particle displacement and does not yet provide strong physical insight [74]. The method of Patinet *et al.* [76] allows for the computation of energy barriers, but it is computationally expensive and not clearly related to the microstructure or linear response.

In this chapter, we develop a new method that pushes phonon-like modes out of the low-frequency spectrum, leaving isolated excitations behind. We find that these localized excitations are excellent predictors of future rearrangements. We also characterize the number density of defects, finding that fewer soft spots are required to make accurate predictions than previously thought.

It also allows us to characterize properties of localized excitations that are usually treated as fit parameters in mesoscopic models, including defect size and the magnitude of associated energy barriers. We find a localization length for defects of approximately 7.3 particle diameters, corresponding to a soft spot containing about 150 particles. To calculate energy barriers, we do not follow existing methods that use the adjacency matrix associated with the contact network to identify saddle points [77] as these can generate false positives [78, 79]. We develop a more robust method and find that defects have lower energy barriers than those for normal modes.

2.2 Simulation Model

We study 50:50 mixtures of 2500 bidisperse disks with diameter ratio 1.4, at a packing fraction of $\phi = 0.9$, significantly larger than the jamming transition at $\phi_J \simeq 0.84$ [37]. Their interaction potential is Hertzian: $V = \frac{2}{5}\kappa\delta^{5/2}$, where δ is the particle overlap. Lengths are in units of the mean particle diameter, and energies are in units of κ . We analyze mechanically stable packings in a periodic box of linear size $L \simeq 50$ generated by an infinite temperature quench [37]. The system is sheared using Lees-Edwards boundary conditions [80].

To find vibrational modes, we use ARPACK [81] to calculate eigenvalues, λ , and eigenvectors, \mathbf{e}_i , of the dynamical matrix, M , which describes the linear response of the packing to particle displacements [82]. At large displacements, broken contacts disrupt the linear response [83], but there is always a well-defined linear regime [9, 84]. In our Hertzian packings at $\phi = 0.9$, we are well within this regime.

To penalize long-range collective motion, we augment the system with an artificial square grid (lattice constant a) of spring-like interactions. These spring-like interactions link the coarse-grained particle motions \tilde{u} , and generate an augmented potential energy \tilde{U} :

$$\tilde{U} = \frac{1}{2} \left(\sum_i^n \sum_j^n \sum_{\alpha}^{x,y} \sum_{\beta}^{x,y} u_{i\alpha} M_{i\alpha j\beta} u_{j\beta} + \sum_k^{g^2} \sum_l^{g^2} \sum_{\gamma}^{x,y} K_{kl} (\tilde{u}_{k\gamma} - \tilde{u}_{l\gamma})^2 \right), \quad (2.1)$$

where i, j are particle indices, k, l are grid point indices, Greek indices represent spatial dimensions, $g = L/a$ is the number of grid points per side, and $\tilde{u}_{k\gamma}$ is a Gaussian weighting

of particle displacements and represents an effective grid point motion as described in Appendix A and illustrated schematically in Fig. 2.1. With this augmented energy $\tilde{U} = U + U^\dagger$, the dynamical matrix is $\tilde{M} = M + M^\dagger$ with

$$M^\dagger = \sum_k^{g^2} \sum_l^{g^2} K_{kl} \delta_{\alpha\beta} (W(i, k)W(j, k) - 2W(i, k)W(j, l) + W(i, l)W(j, l)), \quad (2.2)$$

and

$$W(i, l) = \text{Exp} \left[- \sum_{\eta}^{x,y} (x_{i\eta} - l_{\eta}a)^2 / \sigma^2 \right]. \quad (2.3)$$

We refer to modes associated with U as standard modes and those associated with \tilde{U} as augmented modes. As we have implemented the effective spring network on a square grid, $K_{kl} = K\delta_{k,l\pm 1}$. The “motion” of each grid point (\tilde{u}) is illustrated schematically in Fig. 2.1(a); average displacements in the same direction are penalized.

There are three parameters for the augmentation: the width of the Gaussian weighting for each gridpoint σ , the spacing between grid points a , and the strength of the augmentation K . We do not want the augmented energy to affect the energy of individual particles. As discussed in the appendix, the sum of Gaussians is nearly unity when σ is equal to or larger than a ; therefore we choose $\sigma = a$ for the remainder of this chapter.

We want to choose a such that the augmented energy acts as a high-pass filter, increasing the energy of modes with small wavenumbers. Therefore, we compare the standard (U) and augmented (\tilde{U}) energies associated with a field of displacements that vary in amplitude as a plane wave with wavenumber k . An analytic expression for this quantity is derived in Appendix A. The analytic and numerical results, shown in Fig. 2.2(a), suggest that wavevectors smaller than $\sim L/2a$ are significantly penalized and that there is a systematic decrease in sensitivity as a decreases. To balance these effects, we choose $a = L/7$ for the remainder of this chapter.

A more subtle question is how to balance the magnitude of the augmented energy and the standard energy, which is controlled by the parameter K . We want the augmented energy to be sufficient to push out plane waves, without affecting finer scale structure. To do so, we examine the number of well-localized modes as a function of K , as described in

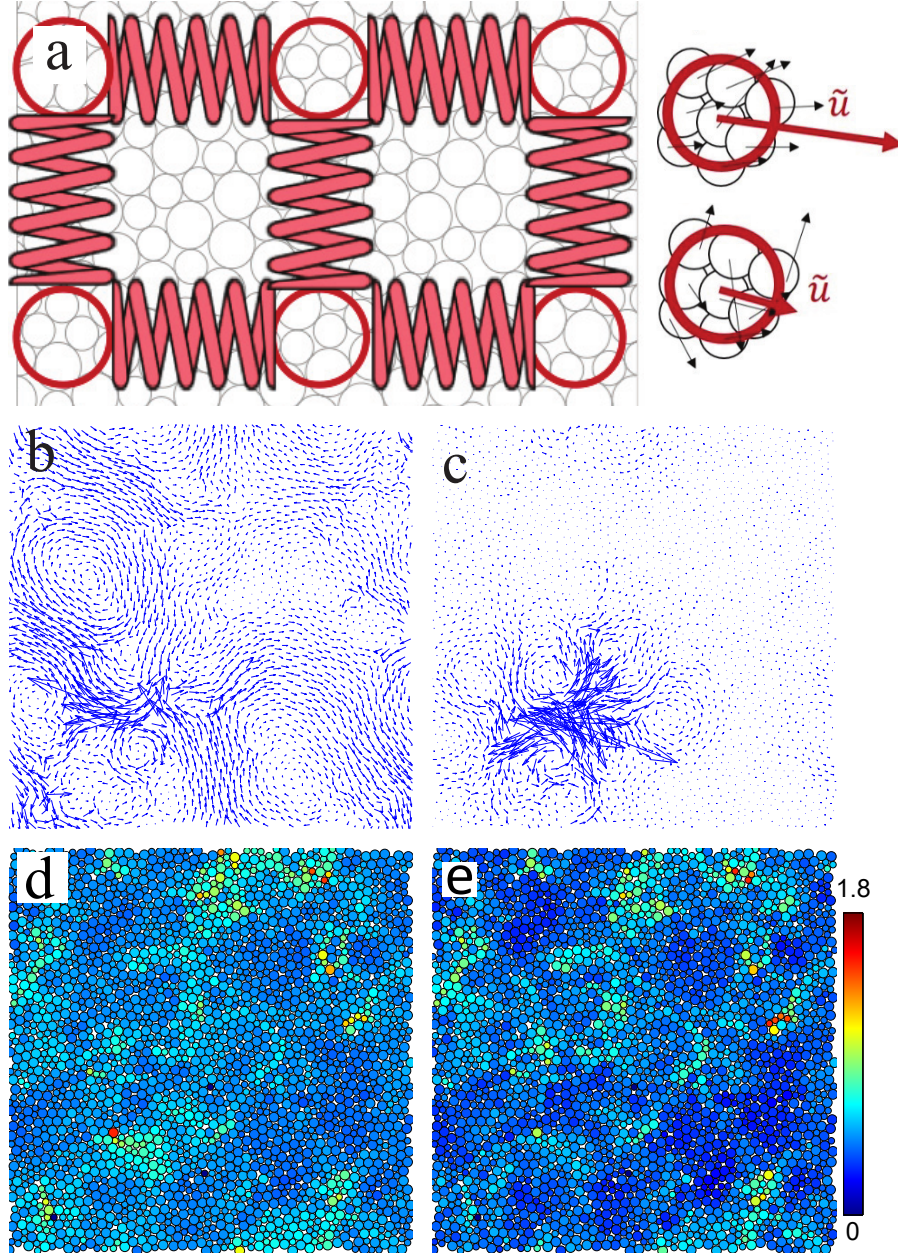


FIGURE 2.1: (a) A square grid of points is connected by a spring-like interaction. Movement of a grid point is defined by the weighted particle displacements. (b) A typical hybridized vibrational mode from a standard dynamical matrix. (c) A typical localized mode from an augmented dynamical matrix. (d,e) The sum of the magnitudes of particle displacements in the 30 standard (d) and augmented (e) modes with the lowest frequencies. The colorbar represents the magnitude of the summed polarization vector.

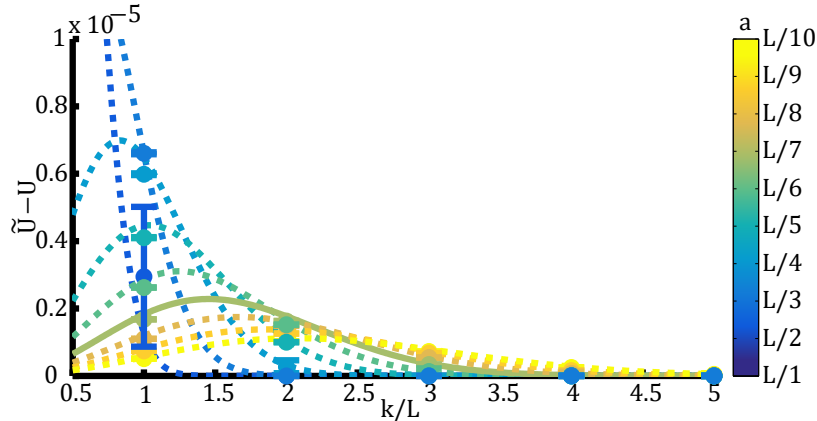


FIGURE 2.2: Energy due to augmentation, $\tilde{U} - U$, of a plane wave of wavenumber k for various number of grid points spacing a ranging from $L/2$ to $L/10$ at $L = 46$. The solid line corresponds to $a = L/7$. Results are shown both for the analytic prediction, as lines, and numerical results, as points, which do not differ significantly.

Appendix B. We find that $K = 0.01$ is sufficient to penalize plane waves without altering the fine-scale structure.

2.3 Results

Having specified reasonable values for a and K , we now explore the eigenspectrum of the augmented system. Fig. 2.1(b) shows the particle displacements in a typical low-frequency hybridized mode derived from the standard dynamical matrix M . A typical low-frequency eigenvector of the augmented dynamical matrix \tilde{M} , shown in Fig. 2.1(c), is localized. The inset shows an exponential decay in amplitude away from the center of the defect, highlighting the absence of long-range quadrupolar tails [11].

Fig. 2.1(d,e) show the sum of the magnitudes of the 30 lowest frequency modes for typical standard and augmented matrices, respectively. In Fig. 2.1(e), large magnitudes occur in the same localized regions as in Fig. 2.1(d), indicating that the augmented potential does not interfere with small-scale structure or alter the locations of the soft spots. The augmentation does suppress the background associated with extended excitations, making soft spots easier to identify.

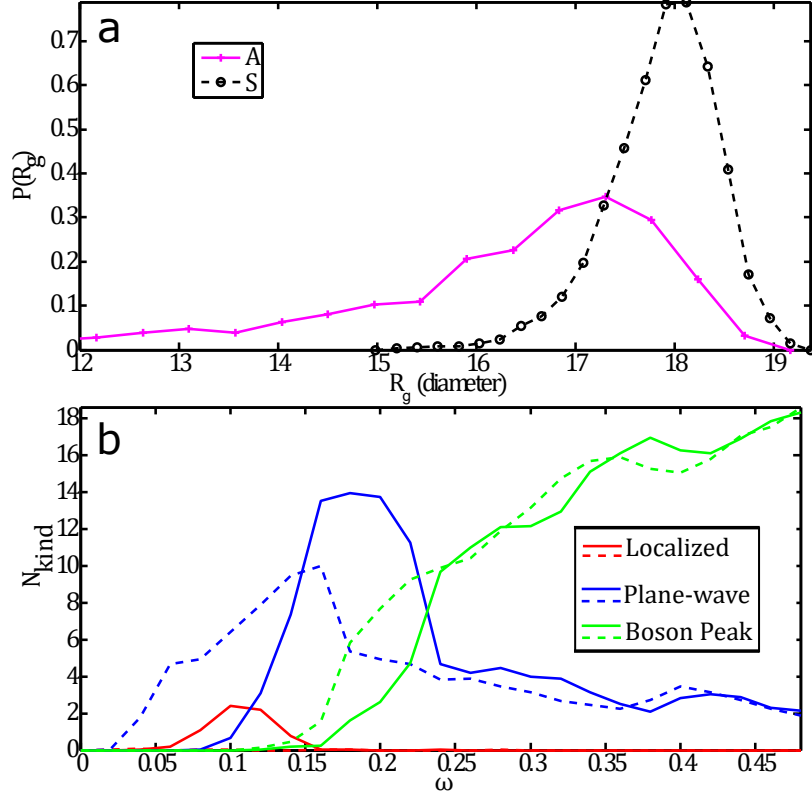


FIGURE 2.3: a) The radius of gyration of the 20 lowest frequency modes in 100 realizations are much smaller for augmented modes (solid line) than for standard modes (dashed line). b) Density of states plotted as number of modes per packing, for augmented (solid) and standard (dashed) modes. Localized modes (red) only appear in the augmented DOS, while the plane waves (blue) in the augmented system have increased energy.

With this choice of parameters we can measure localization with the radius of gyration [85], given by

$$R_g = \sqrt{\frac{\sum_{i=1}^N (|r_i - r_{cm}|^2 |\mathbf{e}_i|)}{\sum_{i=1}^N (|\mathbf{e}_i|)}}. \quad (2.4)$$

To confirm that modes with increased energies are indeed extended, we split eigenvectors into three groups. We find that the normal modes rarely have a $R_G \lesssim 16$ particle diameters as shown in Fig. 2.3a, therefore we denote modes with $R_G < 16$ as “localized”. Remaining modes are characterized by an integral I_f over the Fourier spectrum and L_2 distance L_{BP} between their cumulative distribution functions (cdfs) and the typical boson peak cdf [86]. We find that $I_f = 0.3 - 2.3L_{BP}$ is the best separating plane in $I_f - L_{BP}$ space between “phonon-like” and “boson peak” modes.

Fig. 2.3(b) shows that the augmented potential is altering the spectrum as intended. The augmented eigenspectrum shown by solid lines contains a significant number of localized modes, and plane waves are pushed to higher frequencies compared to standard modes (shown by dashed lines).

2.3.1 Size and number density

In mesoscopic models for plasticity, two important parameters are the number density and size of localized excitations, and therefore one of our goals is to extract distributions for these parameters directly from simulations.

The number of localized augmented modes should serve as a lower bound on the number of localized defects. As seen in Fig. 2.2, our choice of grid spacings suppresses wavenumbers of up to $k \cong 3$ so localized excitations with frequencies above that range will not be isolated. The distribution for the number of localized excitations in our 2D box of 2500 particles is shown in Fig. 2.4a – the average is about 7.

We can also extract a length scale for each localized augmented mode by fitting an exponential function to the decay in displacement amplitude away from the defect center. The distribution of lengthscales associated with these exponential fits is shown in Fig 2.4b, with a mean of 7.89 particle diameters. We have checked that this length is independent of our choice of grid spacing a .

To see how these results compare to previous approaches, we characterize the size and number density of the localized excitations using the soft spots approach [10]. This method identifies clusters of soft particles by grouping together the N_p particles with the largest motion from the lowest N_m frequency modes and optimizes N_p and N_m in order to maximize the correlation C_{sr} of spots with rearrangements. C_{sr} is a very strict criterion comparing the particles that have large displacements in soft spots and rearrangements, respectively.

For standard normal modes at a packing fraction of 0.9, the best correlation with rearrangements is found when we include the $N_m = 25$ lowest frequency modes and the $N_p = 20$ particles in each mode. This corresponds to 14 ± 3 soft spots in each packing of 2500 particles, with an average soft spot size of 14.3 ± 5.7 particles.

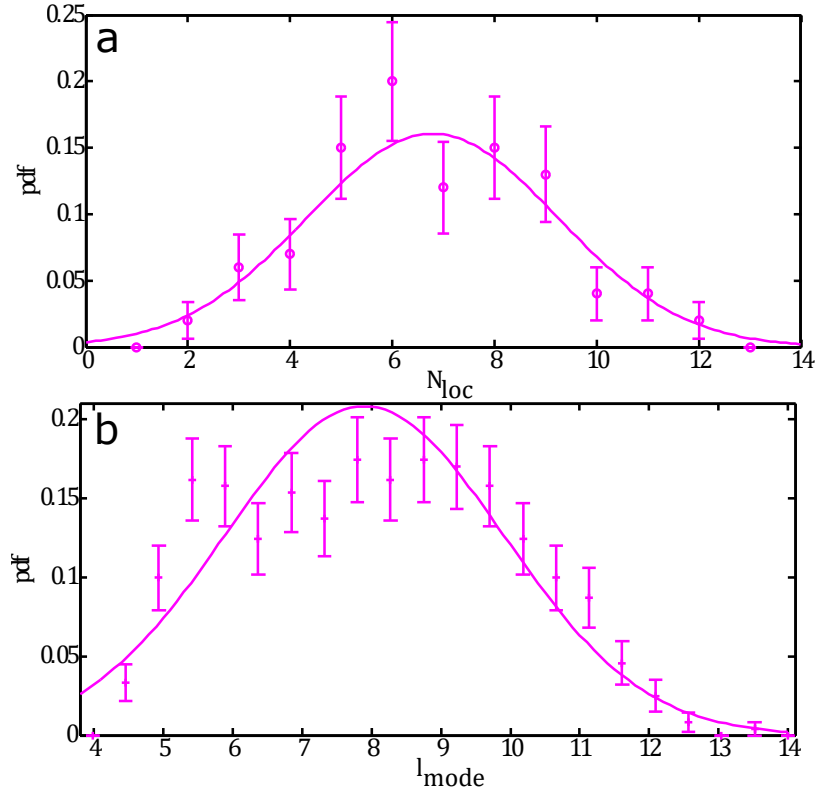


FIGURE 2.4: a) The number of modes with $R_G < 16$ in the augmented system. The line is a Gaussian fit with $\mu = 6.79$ and $\sigma = 2.45$. b) The length scale extracted from an exponential fit to the radially averages distribution of displacement vectors for augmented localized modes. The line is a Gaussian fit with $\mu = 7.89$ and $\sigma = 2.01$.

These results are quite different from those we found with our new augmented approach – the augmented approach finds about half as many localized excitations in the same packing (7 compared to 14) and excitations that are an order of magnitude larger (a lengthscale corresponding to 150 particles compared to 14 particles). Typical defect sizes reported in the literature vary widely and are typically between these two values [6, 22, 87–90].

To unpack this discrepancy, we first look more closely at the size of localized excitations. Fig 2.5 compares displacements in a localized augmented mode to the locations of particles identified by the soft spot algorithm. The soft spot singles out the particles with very large motion during a rearrangement, while the augmented mode retains smaller displacement vectors. Because the defect core is far from compact (perhaps even with string-like structures reported previously [85]), the spatial extent of the soft spot and the localization length (derived from an exponential fit to the displacement field) are actually very similar.

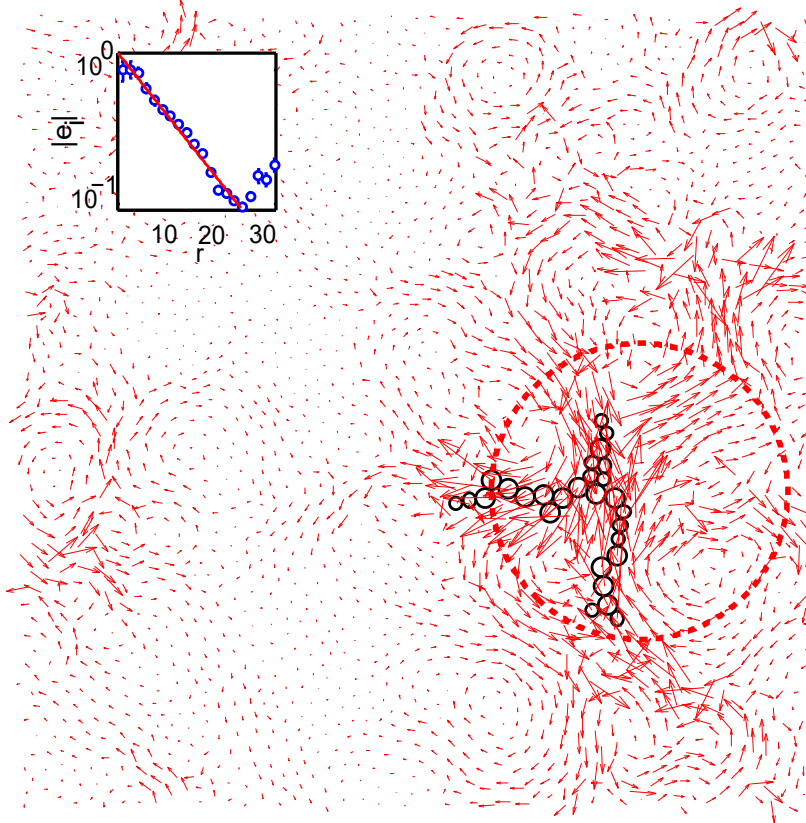


FIGURE 2.5: A soft cluster compared to the most similar augmented mode, of $R_G = 15.3$. The localization length of the augmented mode ($l_{mode} = 8.8$) is represented as a circle. (inset) Blue points are the radially averaged magnitudes of particle displacements $|\mathbf{e}_i|$ at distances r from largest particle displacement; the red line is the best exponential fit.

This suggests that the *size* of a localized excitation may depend quite a bit on how size is measured.

Next, we investigate the number density of localized excitations. A possible weakness of existing soft spots algorithms is that they are only able to demonstrate that a given number of soft spots is sufficient for predicting plasticity, but not that the number is necessary – e.g. these methods may be identifying more spots than are needed to predict rearrangements.

To test this hypothesis, we run the soft spot analysis using only the *localized* augmented modes. As expected, this generates about the same number of soft spots as localized modes (an average of 7 spots). The results are largely insensitive to the number of particles per mode, N_p , for N_p between 20 and 50, as we might have expected from our

analysis of soft spot size above. We report results for $N_p = 25$ so that the average soft spot size matches that for standard modes.

An interesting question is whether the 7 spots identified by our new augmented method are just as effective at predicting plasticity as the 14 spots generated by the old method. Interestingly, the overall average correlation is nearly identical $C_{sr} = 0.777$ for standard modes and $C_{sr} = 0.781$ for localized augmented modes. Fig 2.6(a) shows C_{sr} for standard modes and only localized augmented modes as a function of $\gamma - \gamma_c$, which is the strain required to activate the next rearrangement. We see that close to the event the 7 localized augmented modes are slightly better than the 14 standard soft spots at predicting rearrangements, and nearly as good even far from the event. This suggests that our augmented potential is identifying a subset of localized excitations that predict plasticity and that the number density of such excitations is actually significantly smaller than previously thought.

2.3.2 Direction information and energy barriers

Of course, one of the main benefits of this algorithm is that we can calculate not only the locations of the localized excitations but also the directions of particle motions in an excitation. To see if this directional information is also predictive for particle rearrangements, we take the scalar dot product between each of the localized augmented modes and the rearrangement, as well as the lowest-frequency standard modes. We restrict the dot product to a circular region of radius r_c around the localized event, to avoid noise associated with dot products of many random vectors with small magnitudes. We choose $r_c = L/5$ – which is slightly above the localization length, but results are not highly sensitive to the choice of r_c . We also restrict ourselves to non-avalanche rearrangements, where the rearrangement has over an 80% overlap with the mode that goes to zero at the critical strain [10]. Fig. 2.6 b shows the probability distribution for the highest dot product amongst all modes. There is a much higher probability of finding a dot product near unity for the augmented modes compared to the standard modes, indicating that augmented modes are better predictors of the rearrangement dynamics, even at strains long before a rearrangement event.

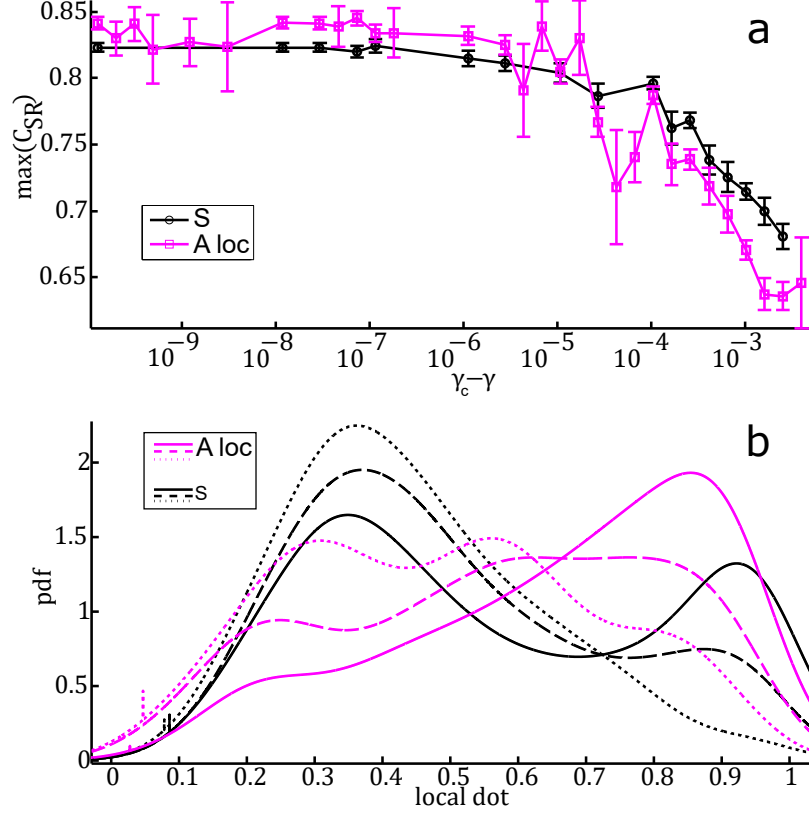


FIGURE 2.6: a) Correlation function C_{SR} between soft spots and rearrangements generated from the localized augmented modes (magenta) are very similar to those for standard modes (black), and more accurate far from the event. Events are binned as a function of the strain required to get to the next particle rearrangement ($\gamma_c - \gamma$). b) Comparison of the highest dot product between localized ($R_G < 16$) augmented modes (magenta) and standard modes (black). The various curves represent different distances in strain from the rearrangement. The solid lines correspond to strains close to a rearrangement ($(\gamma - \gamma_c) < 10^{-4.5}$), the dashed lines are $10^{-4.5} \leq (\gamma - \gamma_c) \leq 10^{-3.5}$, and the dotted line represents $(\gamma - \gamma_c) \geq 10^{-3.5}$. The pdf was created from a cumulative distribution function using a Gaussian smoothing filter of $\sigma = .07$. We see that the localized augmented modes tend to match the rearrangement much better than the standard mode, especially far from the rearrangement as demonstrated by the magenta curves having larger weights near unity.

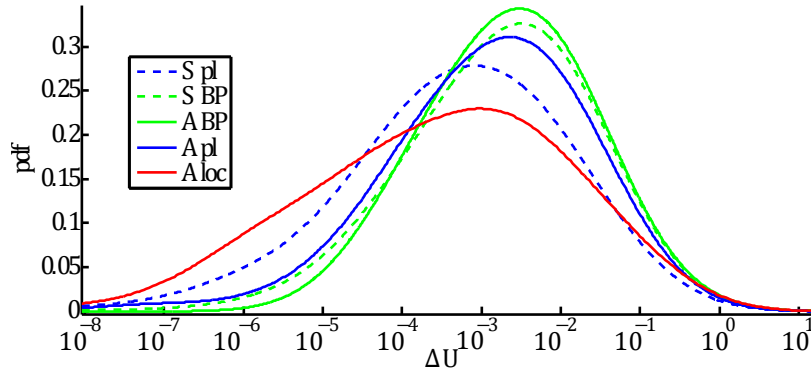


FIGURE 2.7: Probability distribution of energy barrier for standard (dashed), and augmented (solid) modes, collected over the 50 lowest frequency modes in 100 realizations are plotted separated by mode type as in Fig. 2.3. Localized augmented modes are more likely to have very low energy barriers. Curves were produced by smoothing the cumulative distribution function with a Gaussian filter of width 0.7.

This algorithm for the first time allows us to calculate the distribution of energy barriers associated with bare defects. We displace particles along each eigenvector and use the LBFGS line search algorithm [91] to minimize the potential energy at every step. At the first step where the minimized state is different from the initial state, we identify a particle rearrangement and define an energy barrier ΔU as the difference between the initial energy and the maximum energy attained [77].

The definition of a particle rearrangement or new state can be subtle. Although previous studies in particulate matter have used changes in the contact network adjacency matrix to identify energy barriers [77], not all contact changes identify saddle points in the potential energy landscape [9, 78]. In Appendix C, we compare several methods for identifying saddle points in the potential energy landscape, and identify a subset that are self-consistent and match our expectations for saddle points. Using one of these self-consistent definitions, we calculate the energy barriers for the 50 lowest frequency standard and augmented modes over 100 realizations, separated by mode type. Fig. 2.7 shows that the localized augmented modes are more likely to have very low energy barriers compared to standard modes, although the average value is similar.

2.4 Discussion and Conclusions

Using a simple physically-motivated augmented potential, we were able to push extended low-frequency vibrational modes to higher frequencies and isolate localized “bare” defects. We demonstrate that these localized excitations are excellent predictors of both the location and displacements associated with particle rearrangements in a disordered solid. Finally, we characterize the lengthscales, number density, and energy barriers associated with these excitations.

These results should immediately improve continuum models for plasticity in amorphous solids. The energy barriers associated with defects in disordered solids are an important parameter in both STZ and SGR models. While these were previously fitting parameters, one can now extract them from a simulation and test specific model predictions.

A future direction of inquiry is to study the creation, annihilation, and activation of defects in sheared simulations and compare to continuum model assumptions [6, 15, 63, 92–94]. In particular, it would be instructive to use the directional and energy barrier data to predict which defect would activate given a particular shear direction.

We know that other methods for identifying soft spots such as those calculating local yield stress [76], analyzing nonlinear modes [95], or using machine learning [96] also correlate well with particle rearrangements. Therefore, it would be useful to systematically compare these methods on the same packing and determine whether they identify the same localized excitations.

While we have used a multiple contact-change metric for determining a new state to calculate energy barriers, there are many other choices. Ongoing work [78] suggests that all saddle points are accompanied by a drop in stress, while contact changes that are not associated with saddle points do not have a substantial stress drop. We do not use stress drops as an indicator of saddle points here because they are difficult to identify along the non-physical particle paths prescribed by our augmented modes, but we expect this alternate definition to be useful in other systems, such as those under simple shear.

As this method can robustly identify defects far from rearrangements, we are now well poised to study their dynamics. For example, we hope to study the creation and annihilation of defects under shear, and whether their statistical properties (such as the

lengthscale, number density, or energy barrier) are different as a function of material preparation or shearing history. This new technique should also allow us to study the spatial organization of defects in processes such as shear banding that lead to catastrophic failure.

Additionally, it would be interesting to try to extend this algorithm to systems that are not in mechanical equilibrium. For example, during an avalanche, in a highly jammed packing we expect that most of the motion will be along a few floppy modes, so that most of the curvatures in the potential energy landscape are still positive and amenable to study via vibrational mode techniques. This would allow us to observe the activation and formation of defects, to understand if avalanches mostly result from one defect triggering other, pre-existing defects, or if avalanches create and activate new defects.

The self-organization of defects may also provide insight into the reversibility dynamics seen by Keim *et al.* [7, 30, 63]. The evolution of soft spots as a function of time and their organization in the highly reversible system acquired after many cycles might allow a mesoscopic description of memory formation in materials.

2.5 Appendix A

In this Appendix, we derive the augmented dynamical matrix that allows us to separate localized modes from extended plane-wave-like modes at low frequency in a disordered solid. Latin indices are used to label particles and Greek indices to label Cartesian components. All summations are explicit.

The low frequency vibrational modes of a disordered solid contain localized excitations at defects hybridized with extended plane-wave-like modes and are the eigenvectors of the Dynamical matrix $M_{i\alpha j\beta} = \frac{\partial^2 U}{\partial u_{i\alpha} \partial u_{j\beta}}$. In order to examine the bare defects, we must separate these two types of modes. To prevent hybridization, our goal is to increase the energy of the plane-wave-like modes without increasing the energy of the localized modes.

To do this, we add an extra term to the total energy of the packing U that represents a grid of virtual points connected by a spring-like interaction. The motion of each grid point is defined as the motion of the particles near it, weighted by a Gaussian function of the distance between them. The new energy is then

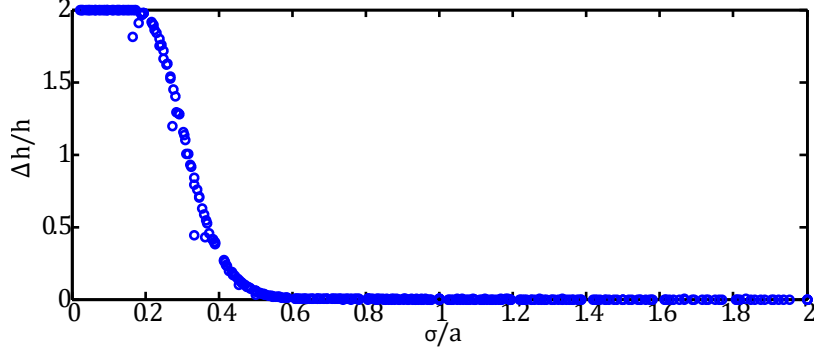


FIGURE 2.8: Ratio of height variation Δh to mean height \bar{h} of a grid of gaussians of width σ and spacing a between each peak.

$$\tilde{U} = \frac{1}{2} \left(\sum_i^n \sum_j^n \sum_{\alpha}^{x,y} \sum_{\beta}^{x,y} u_{i\alpha} M_{i\alpha j\beta} u_{j\beta} + \sum_k^{g^2} \sum_l^{g^2} \sum_{\gamma}^{x,y} K_{kl} (\tilde{u}_{k\gamma} - \tilde{u}_{l\gamma})^2 \right), \quad (2.5)$$

where

$$\tilde{u}_{k\gamma} = \frac{\sum_p^n u_{p\gamma} \text{Exp} \left[-\sum_{\eta}^{x,y} (x_{p\eta} - k_{\eta}a)^2 / \sigma^2 \right]}{\sum_p^n \text{Exp} \left[-\sum_{\eta}^{x,y} (x_{p\eta} - k_{\eta}a)^2 / \sigma^2 \right]}, \quad (2.6)$$

$$k_x = \text{Floor}[k/g], \quad (2.7)$$

$$k_y = \text{Mod}[k, g], \quad (2.8)$$

$$g = L/a, \quad (2.9)$$

where g is the number of grid points per side, a is the spacing between grid points, and L is the side length. K_{kl} sets the connectivity and the strength of the connection between grid points. In this work, we connect adjacent grid points on a square grid, so that $K_{kl} = K\delta_{k,l\pm 1}$.

The width of the Gaussian weighting is set equal to the grid spacing, as the sum of a grid of Gaussians with the width equal to the spacing is flat to within 10^{-6} , as seen in Fig.2.8. We divide by the Gaussian contribution of each particle near the grid point to normalize by particle density.

The total augmented energy can be written as a quadratic function in terms of the standard dynamical matrix M and the dynamical matrix M^\dagger corresponding to the augmented potential:

$$\tilde{U} = \frac{1}{2} \left(\sum_i^n \sum_j^n \sum_\alpha^{x,y} \sum_\beta^{x,y} u_{i\alpha} \left(M_{i\alpha j\beta} + M_{i\alpha j\beta}^\dagger \right) u_{j\beta} \right). \quad (2.10)$$

To simplify notation, we introduce a weighing function

$$W(i, l) = \frac{\text{Exp} \left[-\sum_\eta^{x,y} (x_{i\eta} - l_\eta a)^2 / \sigma^2 \right]}{\sum_p^n \text{Exp} \left[-\sum_\eta^{x,y} (x_{i\eta} - l_\eta a)^2 / \sigma^2 \right]}. \quad (2.11)$$

and then \tilde{U} becomes:

$$\begin{aligned} \tilde{U} = \frac{1}{2} & \left(\sum_i^n \sum_j^n \sum_\alpha^{x,y} \sum_\beta^{x,y} u_{i\alpha} M_{i\alpha j\beta} u_{j\beta} + \sum_k^{g^2} \sum_l^{g^2} \sum_\gamma^{x,y} K_{kl} \left(\left(\sum_p^n u_{p\gamma} W(p, k) \right) \left(\sum_p^n u_{p\gamma} W(p, k) \right) - \right. \right. \\ & \left. \left. 2 \left(\sum_p^n u_{p\gamma} W(p, k) \right) \left(\sum_p^n u_{p\gamma} W(p, l) \right) + \left(\sum_p^n u_{p\gamma} W(p, l) \right) \left(\sum_p^n u_{p\gamma} W(p, l) \right) \right) \right). \end{aligned} \quad (2.12)$$

Without loss of generality, we reindex the summations from p to i and j

$$\begin{aligned} \tilde{U} = \frac{1}{2} & \left(\sum_i^n \sum_j^n \sum_\alpha^{x,y} \sum_\beta^{x,y} u_{i\alpha} M_{i\alpha j\beta} u_{j\beta} + \sum_k^{g^2} \sum_l^{g^2} \sum_\gamma^{x,y} K_{kl} \left(\left(\sum_i^n u_{i\gamma} W(i, k) \right) \left(\sum_j^n u_{j\gamma} W(j, k) \right) - \right. \right. \\ & \left. \left. 2 \left(\sum_i^n u_{i\gamma} W(i, k) \right) \left(\sum_j^n u_{j\gamma} W(j, l) \right) + \left(\sum_i^n u_{i\gamma} W(i, l) \right) \left(\sum_j^n u_{j\gamma} W(j, l) \right) \right) \right). \end{aligned} \quad (2.13)$$

As each term has a sum over i and j , these can be grouped

$$\tilde{U} = \frac{1}{2} \sum_i^n \sum_j^n \left(\sum_{\alpha}^{x,y} \sum_{\beta}^{x,y} u_{i\alpha} M_{i\alpha j\beta} u_{j\beta} + \sum_k^{g^2} \sum_l^{g^2} \sum_{\gamma}^{x,y} K_{kl} u_{i\gamma} u_{j\gamma} \left(W(i, k) W(j, k) - \right. \right. \\ \left. \left. 2W(i, k) W(j, l) + W(i, l) W(j, l) \right) \right). \quad (2.14)$$

We reindex again:

$$\sum_{\gamma} u_{i\gamma} u_{j\gamma} = \sum_{\alpha} u_{i\alpha} u_{j\alpha}, \quad (2.15)$$

$$\sum_{\alpha} u_{i\alpha} u_{j\alpha} = \sum_{\alpha} \sum_{\beta} u_{i\alpha} u_{j\beta} \delta_{\alpha\beta}, \quad (2.16)$$

by definition of Kronecker delta. Grouping the dimension sums and gathering terms we find

$$\tilde{U} = \frac{1}{2} \sum_i^n \sum_j^n \sum_{\alpha}^{x,y} \sum_{\beta}^{x,y} \left(u_{i\alpha} \left(M_{i\alpha j\beta} + \delta_{\alpha\beta} \sum_k^{g^2} \sum_l^{g^2} K_{kl} \left(W(i, k) * W(j, k) - \right. \right. \right. \\ \left. \left. \left. 2W(i, k) * W(j, l) + W(i, l) * W(j, l) \right) \right) u_{j\beta} \right) \quad (2.17)$$

,

resulting in the final definition of M^{\dagger} ,

$$M^{\dagger} = \sum_k^{g^2} \sum_l^{g^2} K_{kl} \delta_{\alpha\beta} \left(W(i, k) W(j, k) - 2W(i, k) W(j, l) + W(i, l) W(j, l) \right). \quad (2.18)$$

We can analytically determine the energy increase for plane waves by assuming a continuous field of particles, which allows us to go from a summation to an integral over

particle positions. We let the plane wave be defined as

$$u_x = A \sin(2\pi kx/L + \phi), u_y = 0. \quad (2.19)$$

Then the continuous form is

$$U^\dagger = \sum_{k_x=1}^{Gt} \sum_{l_x=1}^{Gt} \sum_{k_y=1}^{Gt} \sum_{l_y=1}^{Gt} \left(\delta(l_x, k_x \pm 1) \delta(l_y, k_y \pm 1) K \cdot \int_{-\infty}^{\infty} \int_{-\infty}^{\infty} \left(dx dy \frac{A}{\pi \sigma^2} \sin(2\pi kx/L + \phi) \left(e^{-\frac{(x-ak_x)^2 + (y-ak_y)^2}{\sigma^2}} - e^{-\frac{(x-al_x)^2 + (y-al_y)^2}{\sigma^2}} \right) \right) \right). \quad (2.20)$$

In order to deal with boundary conditions, we take the limit as $Gt \rightarrow \infty$. we also set $\sigma = a$, and $\lambda = L/k$. This computation gives the result

$$U^\dagger = -4\pi^2 A^2 K e^{-\frac{8\pi^4 a^2}{\lambda^2}} \left(\cos\left(\frac{4\pi^2 a}{\lambda}\right) - 1 \right). \quad (2.21)$$

which is shown by the dashed lines in Fig. 2.2 in the main text

2.6 Appendix B

To choose a value for the parameter K , the connection strength, we calculate the total number of localized modes of the 50 lowest frequency modes in the packing as a function of K , where localized modes are defined using the radius of gyration as defined in the main text. As seen in Fig 2.9, the number of localized modes grows until a value of $K = 0.01$ and essentially plateaus thereafter. Additionally, the number of boson peak modes is relatively constant until the same value. Furthermore, the number of plane-wave modes begins a more sharp decline at that value. Taken together, this suggests that a value of $K = 0.01$ balances the augmented energy with the internal potential energy to shift plane waves without generating spurious localized modes.

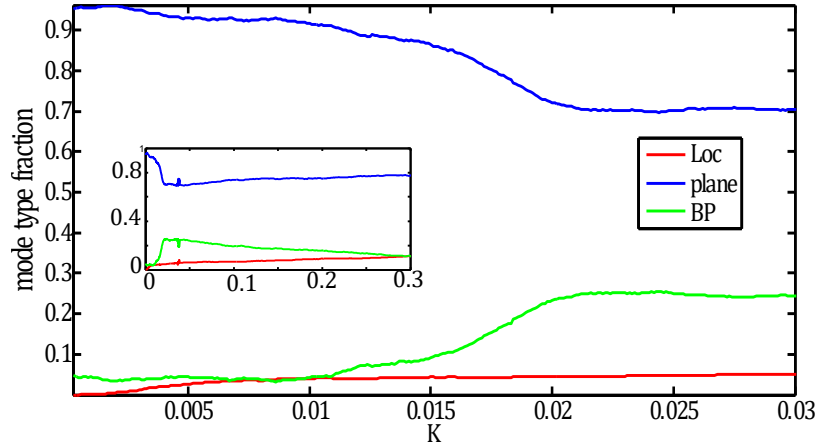


FIGURE 2.9: The 50 lowest frequency modes in 100 packings, sorted by type as in Fig.2.3b, plotted as a function of K . There are three regions: $0 < K < 0.01$, where the augmentation begins to have an effect, $0.01 < K < 0.02$, where the augmentation begins to greatly alter the mode structure, and $0.02 < K$, where the number of spurious localized modes grow linearly with K , as shown in the inset over a wider range of K .

2.7 Appendix C

In order to define a new state, we examine seven independent criteria: i) any change in the contact network (CR+), ii) non-rattler [97] contact changes (CR-), iii) requiring more than two particles to change contacts (C2), iv) energy differences between the original and final basins of greater than 10^{-8} (E-8), v) a displacement of a single particle more than two large particle diameters in a direction perpendicular to the mode (D), vi) having a significant stress drop (S), and vii) requiring that more than 2 contact changing particles must be neighbors, thereby rearranging as a unit, (C2N).

As shown in Fig. 2.10, for each standard mode and each of the first five definitions, we measure the ratio between the energy barrier calculated using that definition and C2N ($\Delta U / \Delta U^{C2N}$). Several of these criteria, such as contact changes that include or exclude rattlers (CR+, CR-), generate energy barriers that are significantly lower than the other criteria and different from each other. We note that these definitions have been used for studies of energy barriers in the past [77]. This result suggests that these criteria generate a lot of “false positives” – they identify changes to the network that do not correspond to a particle rearrangement. In contrast, the four other methods (C2, E-8, D, S) generate distributions of energy barriers with the same median as C2N, indicating

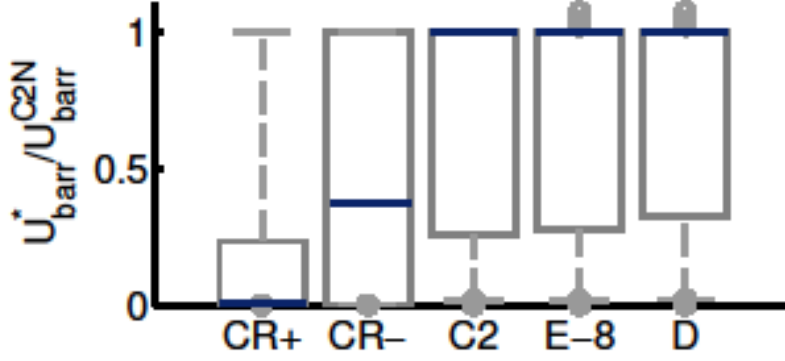


FIGURE 2.10: Ratio of energy barriers $\Delta U / \Delta U^{C2N}$ calculated using different definitions for what constitutes a particle rearrangement, as described in the main text. Box and whiskers contains 50 % and 92 % of the data points, respectively, blue bars denote the median, and outliers are circles.

that these criteria are very similar and likely identify particle rearrangements associated with saddle points and plasticity.

2.8 Appendix D: Defect size and predictive capability

As discussed in the main text, we find that the augmented modes are just as predictive as standard modes if we use the soft spot algorithm to correlate localized excitations with plasticity, and we can use fewer modes (15 augmented modes compared to 25 standard modes).

As a third measure of whether localized excitations predict plastic events, we compare the distance between the center of mass of the localized excitation and the center of mass of the rearrangement.

Of course, we expect that this distance will scale with the number density of candidate defects, so we first calculate the probability density P for the minimum distance r between

the origin and n points randomly distributed in 2D space:

$$P(r, n) = 2\pi nr \Theta\left(\frac{1}{2} - r\right) (1 - \pi r^2)^{n-1} - n \Theta\left(r - \frac{1}{2}\right) \\ * \left(-\frac{4r}{\sqrt{4r^2 - 1}} + \frac{4}{\sqrt{4 - \frac{1}{r^2}}} + 2r(\pi - 4 \csc^{-1}(2r)) \right) \\ * \left(-\sqrt{4r^2 - 1} + r^2(\pi - 4 \csc^{-1}(2r)) + 1 \right)^{n-1}, \quad (2.22)$$

where Θ is the Heavyside function. The expected minimum distance for n randomly distributed points is then $d_{rand}^n = \int r P(r, n) dr$.

Given the location of the center of a rearrangement and a list of n locations corresponding to centers of localized excitations, we compute the minimum distance between the rearrangement and any localized excitation d^n . We then normalize d^n by the value of a random distribution, d_{rand}^n , and if our rearrangements are predictive than $d \equiv d^n / d_{rand}^n < 1$, and there is no bias as a function of the number or size of the localized regions.

We compare the distributions of d for several different definitions of localized excitations. We first assume every localized augmented mode corresponds to a defect, and compare d just before (at a strain 10^{-6} below the critical strain) the event (denoted 'near'), as well as immediately after the previous rearrangement (far). We repeat this procedure for the standard modes and soft spots generated by the method of Manning and Liu [15].

As shown in Fig. 2.11, using this strict metric, the augmented modes display significant improvement over a random distribution with the same number of candidates. The augmented modes are also closer in distance to the rearrangement than soft spots once controlled for the number of candidates.

As discussed in the main text, we also want to understand how the size of localized augmented excitations compares to the size of soft spots. To this end, we use the published soft spots algorithm to identify the optimal number of modes ($N_m = 25$) and number of particles ($N_p = 20$). A histogram for the number of spots and their size are shown by the black data points in Fig. 2.12 a and b, respectively. Next, we only study soft spots generated from localized augmented modes, and since there are only 7 such modes we expect to find approximately that number of soft spots, which is the case, as shown by the red and magenta data points in Fig 2.12a. The correlation with rearrangements is

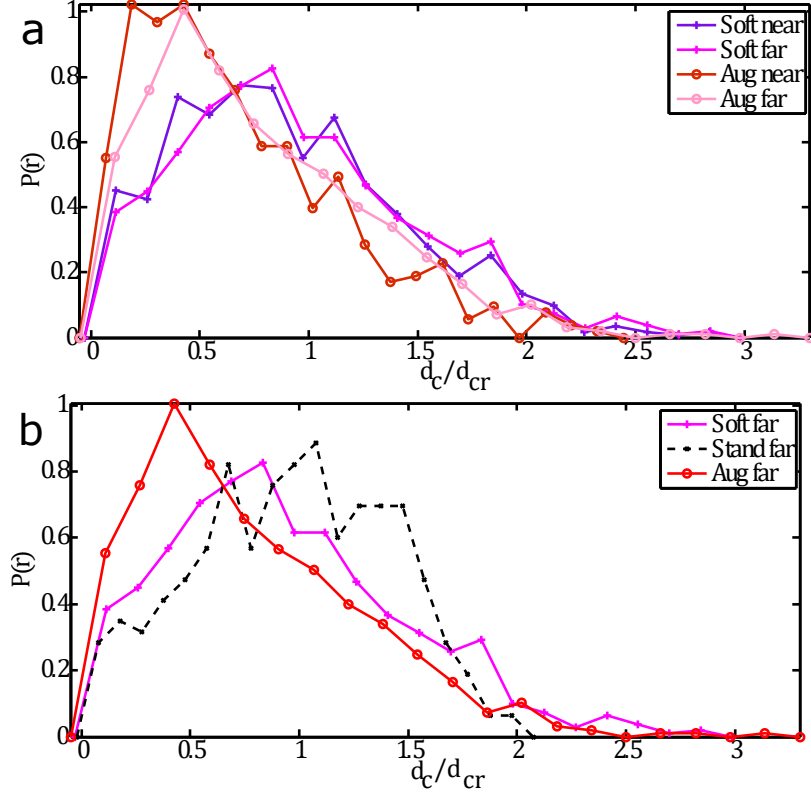


FIGURE 2.11: Comparison of the separation distances between the center of a mode and the center of a rearrangement. We compare standard modes, augmented modes, and soft spots, near and far from the rearrangement, as well as a comparison to a random distribution of the same number as described in Appendix C. Each line is scaled by the expected value of a random distribution of the same number of candidates.

largely insensitive to N_p for values between 20 and 30, but N_p does affect soft spot size, as shown in Fig. 2.12b.

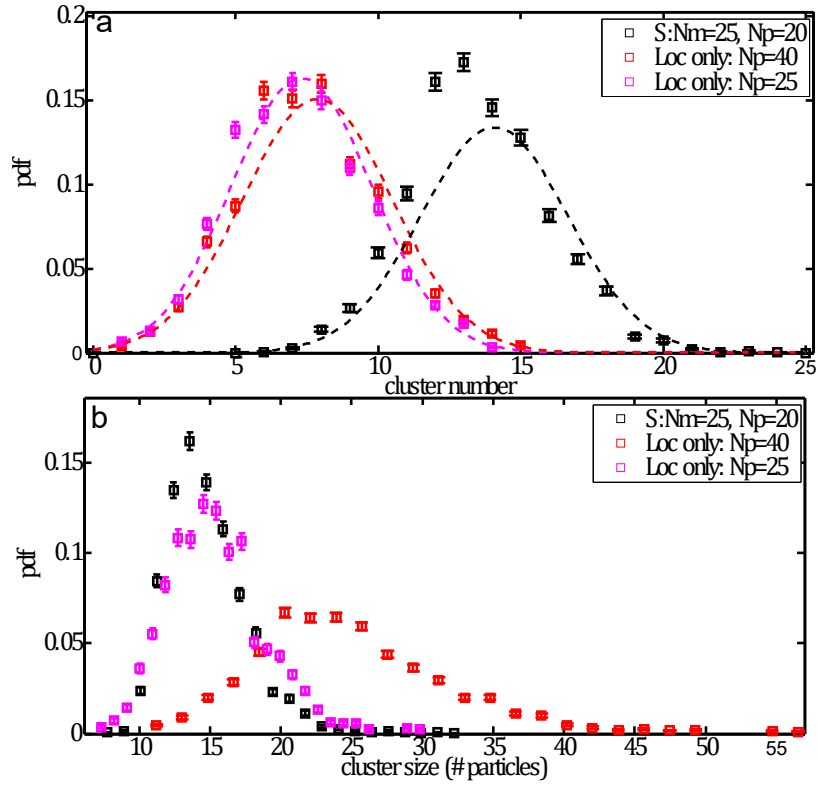


FIGURE 2.12: a) The number of clusters for the standard soft spots algorithm (black), as well as when using only the localized augmented modes ($R_G < 16$), with $N_p = 25$ (magenta) and $N_p = 40$ (red). Using only the localized modes gives fewer spots. Dashed lines are Gaussian fits. b) The average number of particles per soft spot. Colors are same as in a).

Chapter 3

Distinguishing rearrangement events in disordered solids as a function of pressure [†]

3.1 Introduction

While all solids resist shear deformations, they will begin to weaken and flow if a large enough shear stress is applied. In disordered solids such as granular materials, foams, and dense colloids, the mechanisms for flow and failure vary widely as a function of material preparation and the type of applied stress and remain poorly understood. On the macroscopic scale, solids can weaken via a reduced elastic modulus [9] or fail via localized rearrangements [10], sporadic large-scale avalanches [11–13], or continuously evolving extended shear bands [14–17].

To make predictions about such large-scale failure mechanisms, many continuum models [22, 26–29] make assumptions about the statistics of a solid’s complex potential energy

[†] This chapter is part of an ongoing collaboration with Martin van Hecke, Merlijn van Deen, and Peter Morse. This work initiated a manuscript in preparation on this topic. [78]

landscape and how applied shear stress drives the system to explore mechanically stable minima within that landscape.

In addition, recent experiments and simulations suggest that particle rearrangements in periodically strained disordered solids can encode memories that can be read out using a proper strain protocol[23, 30]. Interestingly, several details of these memories (including their robustness to noise) appear to depend on the interaction potential and corresponding properties of the potential energy landscape. Furthermore, the ability to encode memories has been tightly linked with the reversibility of rearrangement events.

For these reasons, it is critically important to characterize the elementary particle rearrangements that allow a solid to explore different mechanically stable states. However, there is no universally-accepted definition of when a particle packing has crossed to a “different state”. This was already discussed in Chapter 2, where we wanted to define an energy barrier for localized excitations.

In granular systems where the interaction potential is zero if two particles are not touching—such as a Harmonic potential— it is common to define a rearrangement event as a change to the particle contact network [3, 9, 98]. An additional complication is whether to include rattlers – particles that are not constrained by the rigid backbone of the solid – in the definition of network changes.

In either case, packings before and after a discrete contact change necessarily possess distinct force contact networks, and it has been shown that the nonlinear rheology – the dependence of the bulk modulus on the applied strain – is altered during a contact change [9]. For these reasons, it has often been assumed that the packings before and after a contact change correspond to different minima in the potential energy landscape, separated by an energy barrier [3, 98]. However, this seems to be contradicted by the observation that contact changes are not sufficient to drive the system towards an instability associated with a negative modulus or zero-frequency modes [3, 11, 11, 62, 99].

In addition, it is unclear how the concept of contact changes might be generalized in systems with attractive or non-contact potentials (such as Lennard-Jones). In these systems, particle rearrangements have been associated with stress drops and local shear modulus [100].

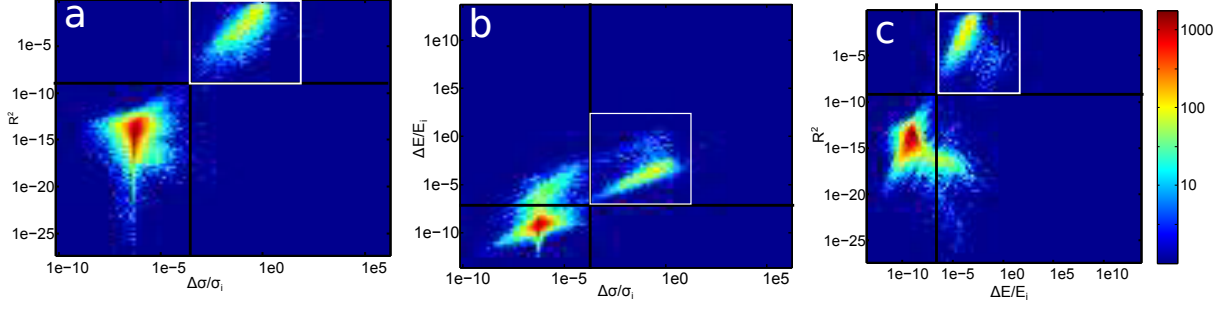


FIGURE 3.1: a) A 2D histogram of the stress drop/initial stress vs the rsq displacement of the particles during an event. There are two clear lobes: the upper right corresponds to a physical event. b) A 2D histogram of the stress drop/initial stress vs the energy drop/initial energy during an event. There are two clear lobes: the upper right corresponds to a physical event. c) A 2D histogram of the energy drop/initial energy vs the rsq displacement of the particles during an event. There are two clear lobes: the upper right corresponds to a physical event. The colorbar represents log number of events in each bin. All events that result in a new relaxed state occur in the white boxes.

Furthermore, the behavior of materials under periodic strain suggests that macroscopic properties depend on whether elementary shear transformations are reversible or not [7, 62, 63]: under a periodic loop of applied strain a shear transformation can be (a) irreversible: particles end up in a different position from where they started, (b) loop reversible: particles end up in the same position but go back via a different path, or (c) line reversible: particles end up in the same position and traverse the same path. Identifying these different types of rearrangement events might help generate predictive models for memory in disordered solids.

Therefore, the goal of this Chapter is to use a simple model granular solid to identify distinct classes of particle rearrangements that correspond to new mechanical states. We would like to understand the properties of these events (such as their degree of spatial localization), and how the frequency of each type depends on control variables such as the strain and pressure.

We find two major categories of rearrangement events, which we denote “rearrangement” and “network”, for convenience. “Rearrangement” events are shear transformation events associated with measurably non-zero changes in shear stress, energy, and particle positions. “Network” events correspond to simple changes in the contact network, with no associated changes in the stress, energy, or particle positions.

We further divide both categories into five mutually exclusive event types. Events can either be line reversible, loop reversible, or irreversible. We find network events are either line reversible or irreversible while rearrangement events can be any of the three reversibility types. As we describe below, this classification is useful because the degree of localization and the relative fractions of each event type change drastically as a function of pressure, revealing two distinct regimes: a fragile low-pressure regime dominated by extended, irreversible events and a robust high-pressure regime dominated by reversible, more localized events.

3.2 Methods

Unless otherwise noted, we study 50:50 mixtures of 512 bidisperse disks with diameter ratio 1.4, under Lees-Edwards boundary conditions at a number of packing fractions above jamming $\phi_J \simeq 0.84$ [37]. Their interaction potential is harmonic: $V = \frac{1}{2}\kappa\delta^2$, where δ is the particle overlap. Lengths are in units of the mean particle diameter, and energies are in units of κ . We generate 100 shear-stabilized packings [9] at each pressure studied, which we vary from $P = 10^{-7}$ to 2×10^{-1} . Pressure scales with packing fraction as $P \sim |\phi - \phi_J|^{1.08}$ [101] for this harmonic system, and such shear stabilized packings have zero residual shear stress [102]. We apply quasi-static simple shear using Lees-Edwards boundary conditions.[103] We denote strain that moves the top boundary to the right as “positive strain”.

Individual contact changes are identified using a bisection algorithm with an accuracy $\delta\gamma/\gamma^* < 10^{-6}$, as described in [9]. This algorithm is used to generate 25 events per packing at most pressures, with an additional 75 events studied at the lowest pressures to improve the signal to noise ratio in that regime. We find that contact changes are required for all rearrangement events; for example, we never find a drop in the total energy without a contact change. Therefore, we tag all strain steps where a contact change occurs and proceed to categorize these events.

3.3 Contact changes

For each contact change event, we can calculate the change in shear stress $\Delta\sigma$, total system energy ΔE , and particle positions R^2 . R^2 is defined as the sum of the squares of the differences in the individual particle positions before and after the event. In order to collapse our results, we look at the ratio between the magnitude of the change in stress (or energy) and the initial stress σ_i or energy E_i .

Our first important observation is that a large fraction of contact change events does not generate an instability that leads to a stress or energy drop. As seen in Figure 3.1, there is a clear separation between events that have a measurably non-zero stress drop, energy drop, and particle displacement, and those that do not. This clustering serves as good criteria for determining a “rearrangement” event; in each panel, we have drawn two black lines separating the clusters into exclusive definitions of rearrangement and network events.

The white box in each panel of Figure 3.1 contains every rearrangement event; the fact that the white boxes match up with the black lines demonstrates that measurable changes to the stress are always accompanied by measurable changes to the energy and particle positions as well.

Because all rearrangement events are accompanied by a contact change, we can also study the number of particles that change neighbors in a rearrangement event. Interestingly, a contact change involving only two particles can generate a rearrangement event; shear transformations or T1s typically associated with four or more particles changing contact are not required.

3.4 Stress relaxation

How can we reconcile the fact that contact changes necessarily alter the force contact network with our observation most contact changes do not change the stress or energy state of the system? One hint is given by identifying each contact network with its relaxed state. Specifically, we associate each packing configuration and its contact network

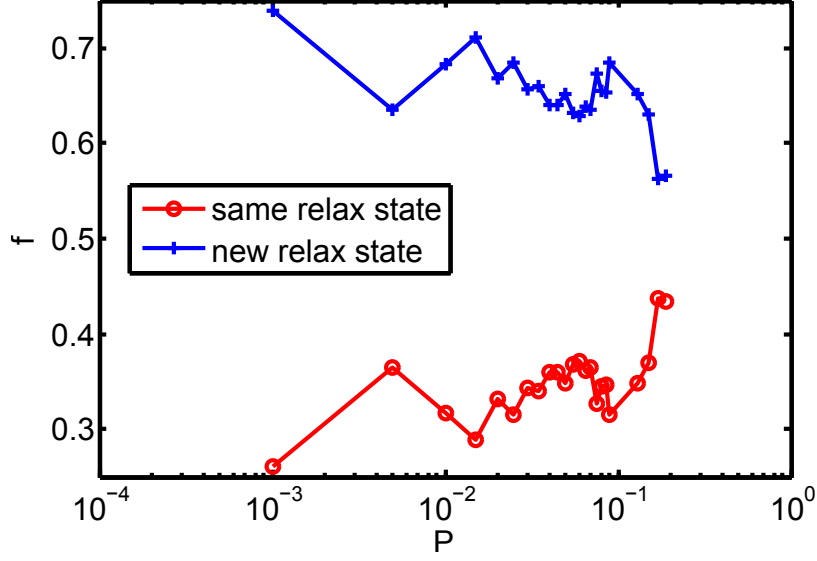


FIGURE 3.2: The fraction of rearrangements that relax to the same (red) or different (blue) state under minimization at zero stress as a function of pressure for a 128 particle system.

with a zero-stress relaxed state, generated by minimizing the energy while the boundary conditions are allowed to evolve freely.

We find that the relaxed state of a packing before a network event is always identical to the relaxed state of packing after that event. This suggests that for network events the two particle configurations on either side of the event are in the same energy basin – there is a flat path in the potential energy landscape between the two configurations that is accessible when the boundaries are allowed to freely evolve.

Interestingly, it is possible for two configurations on either side of a rearrangement event to correspond to the same relaxed state as well. Fig. 3.2 shows that about 30% of rearrangement events are bookended by configurations with the same relaxed state, while the remaining 70% correspond to configurations with different relaxed states, though the exact percentage varies systematically with pressure. By definition, during a rearrangement event, one configuration is driven towards another through a specific path in coordinate space defined by the Lees-Edwards boundary conditions, encountering an energy barrier along that path. However, our results suggest that these states are not always separated by an energy barrier when the boundary conditions are allowed to freely evolve.

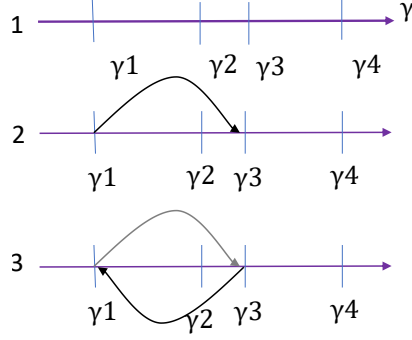


FIGURE 3.3: Step 1: complete a forwards strain sweep, and identify rearrangement events. Step 2: Load in packing from after event at γ_1 , and strain till before γ_3 . Step 3: Strain backwards to the original leading strain.

3.5 Strain reversibility

Next, we want to categorize all events by their reversibility under periodic strain. Specifically, after we have identified an event that occurs under positive strain, we load in the packing after that event. We then strain forwards through an event and stop before the subsequent event. We then strain backwards, called the "reverse path", using the same strain steps until the original strain is reached, which allows us to directly compare the packing at the same values of strain along each path.

For example, as diagrammed in Fig. 3.3, if we wish to investigate an event at some strain γ_2 , we note the strains of the preceding event at γ_1 and the following event at γ_3 . The system is loaded at state γ_1^+ : the closest strain to the preceding event that occurs after that event has taken place. The system is then strained to a strain of γ_3^- : the closest strain to the following event that occurs before the event has taken place.

To quantify if the event was reversible or irreversible, we first measure the return distance Δr , defined as the mean of the sum of the square of each particle's net displacement from the beginning to end of the strain cycle. To determine if events are loop or line reversible, we track the positions of each particle during the loop. At each value of the strain, we examine the difference between the particle positions for the forward and reverse paths, and evaluate the max loop distance M , defined to be the mean of the largest $d = 5$ net displacements, though the results are similar for other values $d < 10$. This measure has the same units as Δr , and thus is ideal for comparison.

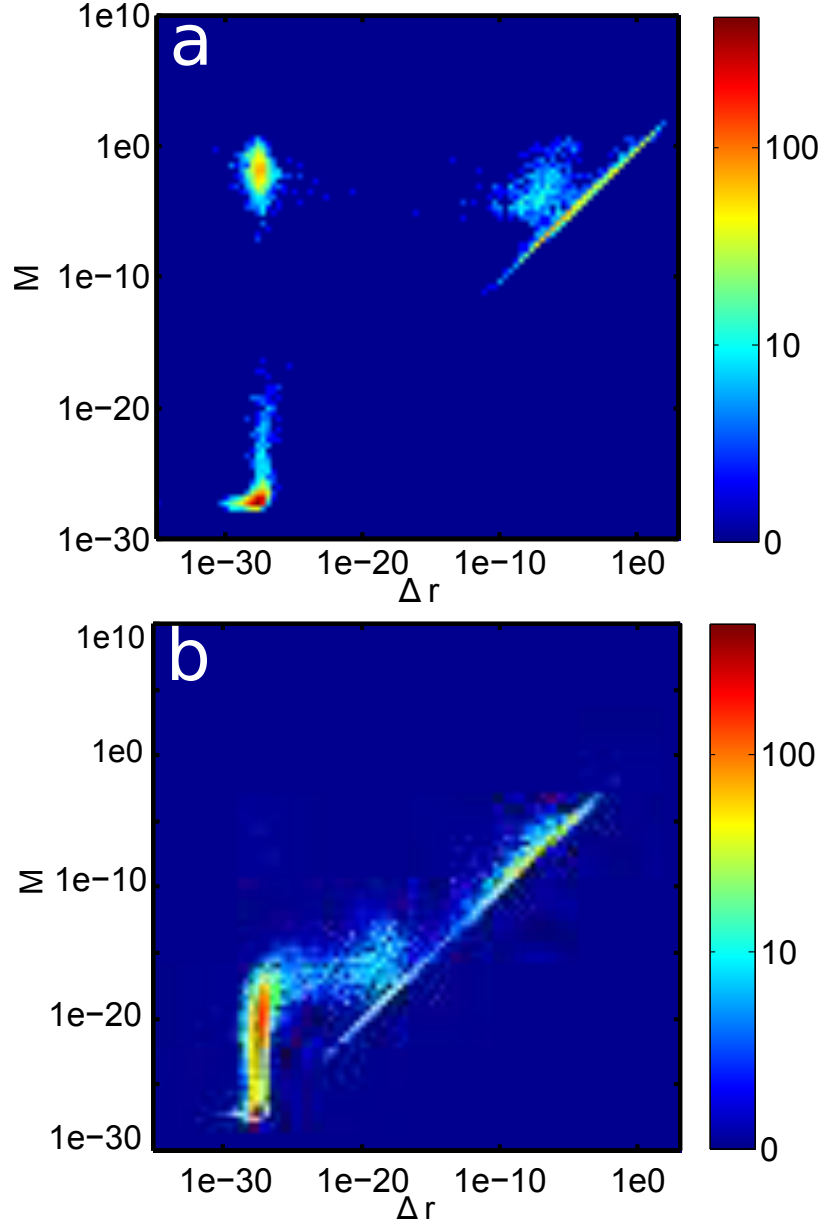


FIGURE 3.4: a) Every rearrangement event binned as a function of the return distance Δr and max loop distance M , as described in the main text. Three clear regimes separate the events into irreversible (upper right), loop reversible (upper left) and line reversible (lower left). b) Every network event binned as a function of the return distance Δr and max loop distance M , as described in the main text. Three clear regimes separate the events into irreversible (upper right), loop reversible (upper left) and line reversible (lower left).

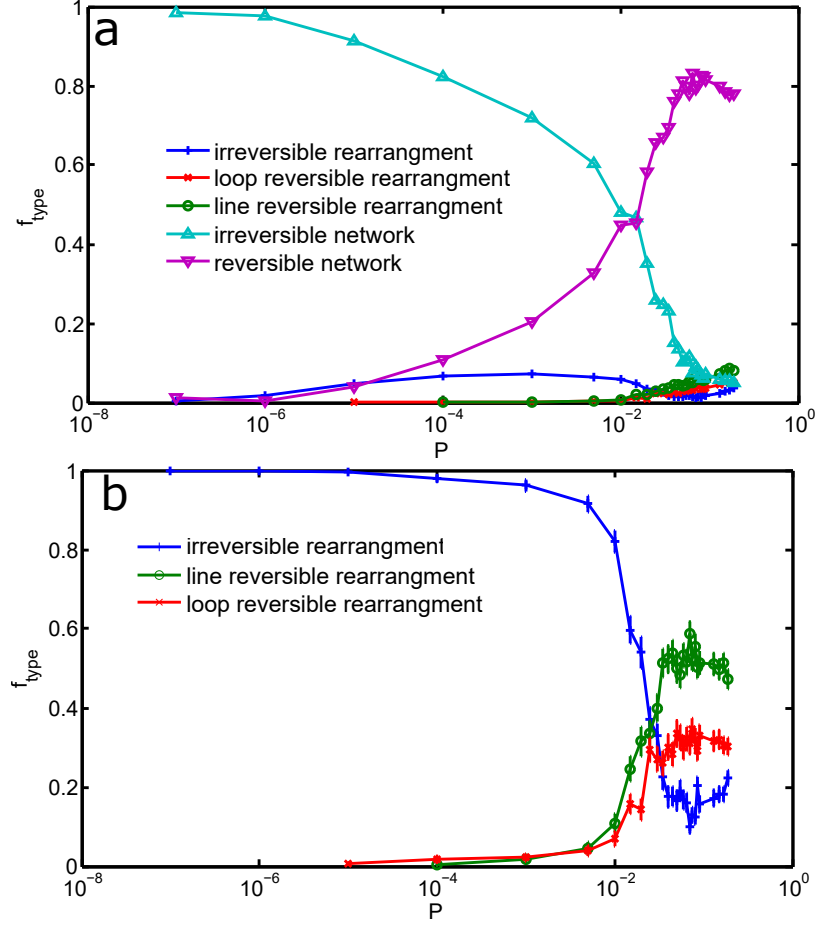


FIGURE 3.5: a) The fraction of irreversible rearrangement(+), line reversible rearrangement (o) loop reversible rearrangement (x), irreversible network (Δ) and reversible network (∇) events to total rearrangement events as a function of pressure. Error bars are smaller than symbols. b) The fraction of irreversible(+), line reversible(o) and loop reversible (x) events to total rearrangement events as a function of pressure. Error bars are smaller than symbols.

As seen in Fig. 3.4a, these two metrics are sufficient to separate all rearrangement events into three clusters: high Δr and high M are irreversible, high M and low Δr are loop reversible, and low Δr and low M are line reversible. There are, and can be, no events that have high M and low Δr . Fig 3.4b demonstrates that there are no loop reversible network events.

Next, we study how the relative fraction of each of the five event types depends on pressure as shown in Fig.3.5. Fig.3.5a shows all five event types, while Fig.3.5b shows just the relative fractions of macroscopic events.

A first observation is that network events are significantly more common than rearrangement events at all pressures accounting for more than 90% of all events. This confirms that studies using contact changes to identify different states are looking at a very different subset of events than those using physical parameters such as energy dissipation or particle displacements to identify different states.

A second observation is that there appear to be two distinct regimes as a function of pressure: a low-pressure regime ($P < 10^{-2}$ in natural units) dominated by irreversible events and a high-pressure regime dominated by reversible ones.

This suggests that the fragility of the system near jamming suppresses reversibility: there are many mechanically stable states with similarly low energies, and therefore any contact change disrupts the structure enough to allow it to find a different state upon reversal. At high pressures the rigid backbone is much more robust, suggesting that there are only a few accessible states with low energy barriers and therefore contact changes are not enough to alter the final state. In fact, for both rearrangement and network events, it is much more common for particles to take the same path forwards and backward (line reversible) than any other path back to the same initial state (loop reversible).

The picture that irreversibility is enhanced by the fragility near the critical jamming point is corroborated by recent work for particle packings at densities below jamming; Schreck and coworkers also see a peak in irreversibility at the critical point [3].

An obvious question is whether fragility and irreversibility are related to the spatial organization of particle displacements during a rearrangement event. Therefore, we characterize the localization of each event using two metrics: the participation ratio and the radius of gyration of the particle displacement field. While the participation ratio is a standard metric for localization[104], we calculate the radius of gyration by first associating the magnitude of each particle displacement during the event with a mass located at the particle position before the event, using a standard method to identify the center of mass [105], and calculating the radius of gyration about that center [85].

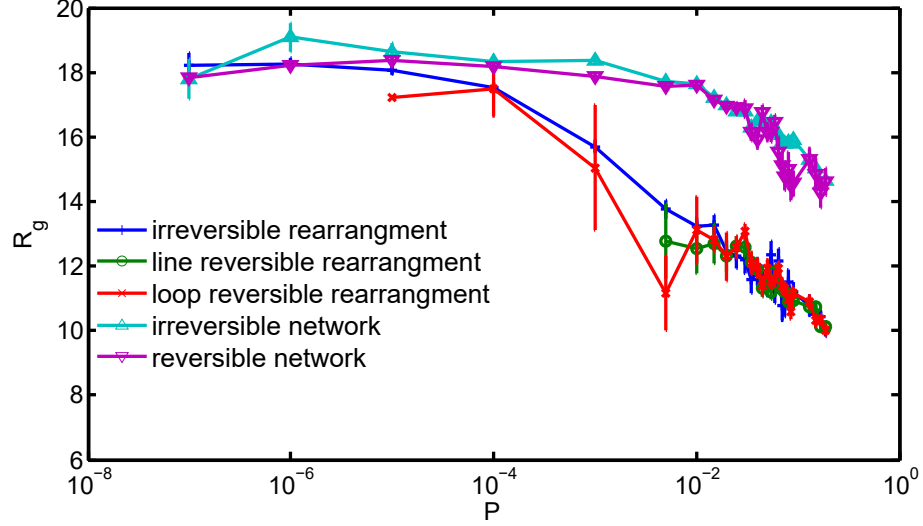


FIGURE 3.6: The size of an event is calculated by using the radius of gyration around the center of mass, where the magnitude of the particle displacement is used for mass in both equations.

3.6 Event size

As seen in Fig.3.6, the spatial extent of all event types plateaus at a constant value for $P \lesssim 10^{-4}$, and decreases thereafter, illustrating that at higher pressures all events become spatially localized. Although rearrangement events decrease gradually with pressure for $P \gtrsim 10^{-4}$, extended network events begin to fall off very quickly for $P \gtrsim 10^{-2}$, which corresponds to the reversible/irreversible crossover.

Overall, Fig.3.6 suggests that spatial organization of displacements correlates strongly with reversibility. At low pressures, displacements are extended because the network is fragile with extended low-frequency normal modes [106]. These extended displacements are not reversible. At high pressures, the system only fails at localized soft spots, and these same spots seem to flip back and forth as the strain is reversed.

3.7 Conclusion and outlook

We have shown that in granular systems, rearrangements that alter the total energy or shear stress in a system, denoted rearrangement events, are much rarer than network

events that alter the contact network but leave the energy unchanged. An analysis of zero-stress states suggests that configurations separated by network events may not correspond to distinct energy basins in the potential energy landscape, as has been assumed in previous work. Furthermore, for both network and rearrangement events, we find a strong connection between reversibility, spatial localization, and pressure. At low pressures, rearrangements are irreversible and spatially extended, while at high pressures they are reversible and spatially localized.

This opens up several future avenues for research. First, it suggests that different continuum models for rheology are appropriate in different pressure regimes. Above $P \approx 10^{-2}$ rearrangements are localized, robust, and reversible, in line with many of the assumptions of Shear Transformation Zone theories [22, 24]. Below $P \approx 10^{-2}$, rearrangements are extended, fragile, and irreversible, suggesting that a scaling theory for low-frequency normal modes [36, 75, 95, 107, 108] may capture many of the important features.

Postdoctoral associate Peter Morse has continued to study these protocols and has found similar results. He has developed a more sensitive criteria for network events based on stress drop as a function of pressure, as shown in Fig.3.7. We expect that this new definition may alter some of the results reported here, although we expect this analysis to guide future work.

It will also be useful to think about which regimes are important for various oscillatory strain protocols, and whether memory formation and readout are more effective in one regime compared to another.

This analysis can be extended to frictional systems and systems with different particle shapes. It will be interesting to see if the sharp crossover between the reversible and irreversible regimes still exists in these perturbed systems, and whether the location of the crossover changes.

So far, we have restricted ourselves to studying particle packings that are not strained very far (less than 5%) from a zero-stress state. Therefore, we are unlikely to see large avalanches associated with self-organized states that occur when the average shear stress is comparable to the average pressure. It will be interesting to study how reversibility is affected by the average shear stress in addition to the pressure.

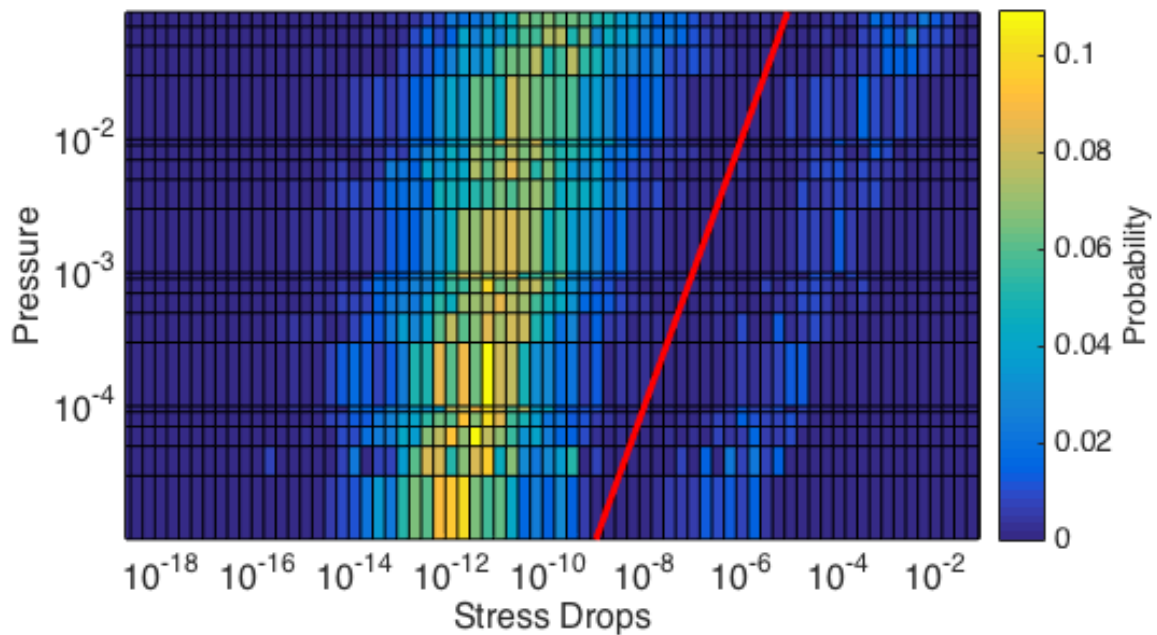


FIGURE 3.7: Histogram illustrating frequency of stress drops as a function of pressure. The red line is the best separating plane between network events and rearrangements with $S \approx 10^{-5}P$.

We thank Giuseppe Passucci for discussions. M.L.M. and S.W. were supported by NSF-DMR-1352184, and M.L.M. was supported by the Alfred P. Sloan Foundation.

Chapter 4

Conclusion

4.1 Summary

In summary, we have developed an algorithm that is able to determine the soft spots in a disordered material, and therefore predict the sites of rearrangement, as well as predicting the displacement directions and energy barriers for defect activation and particle rearrangements. This method, though used here only for a 2D Hertzian contact potential system, is easily generalizable to any system for which a dynamical matrix can be calculated.

Additionally, we have shown that most contact change events are not defect activations, but network events that only change the bulk modulus, but not the generalized energy basin of the system. This tells us that contact changes do not define a new state. Despite the reasoning that we should expect topological differences in the contact network to be different basins in the energy landscape, the true measure of a new state is a stress drop, or equivalently an eigenvalue going to zero.

The metric for events that change the state of the system is conclusively found in Chapter 3 to be stress drops. However, this is not the metric used in Chapter 2 to define the energy barriers. Why the difference? Stress is a well-defined metric when states are at their energy minimums; the states creating during the energy-barrier finding procedure are deliberately unstable and the stress is not well defined.

4.2 Outlook

We have observed that all rearrangement events are predicted by a soft spot. While we did not explicitly check network events, they may also be predicted by soft spots, though we would expect the spot to persist through the event.

All the tools are now in place to look at the time evolution and dynamics of defects. Our method allows the direct calculation of energy barriers associated with defects in disordered solids, an important parameter in both STZ and SGR models. A future direction of inquiry is to study the creation, annihilation, and activation of defects in sheared simulations and compare to continuum model assumptions [6, 15, 63, 92–94]. In particular, it would be instructive to use the directional and energy barrier data to predict which defect would activate given a particular shear direction.

Observing the creation and annihilation rates of defects would provide instructive parameters for STZ and other continuum models for glassy dynamics. In fact, we now have the ability to generate all the parameters in Eqs. 1.6–1.13. While these were previously fitting parameters, one can now extract them from a simulation and test specific model predictions. Our method can measure creation rates, transition rates, orientation, and energy barrier for the STZs in a packing. These parameters can directly be used in the STZ equations of motion to analytically derive the stress-strain relation, which can be directly compared to the simulation. We feel this would be a strong test for STZ theory.

We are also able to test the protocol dependence suggested by Gendelman *et al.* [109], who show that even small changes in the shear direction can alter where the packing deforms. Our method is able to predict all potential rearrangement sites, and thus show that defects are part of the inherent structure. A similar methodology could find a relation between the orientation of the activated defect and the strain angle.

It is known that packings at cyclic shear with a low strain amplitude settle into a reversible steady-state [7]. Given that such systems encode memory[30], it is likely that the defect statistics between the steady state and the uncycled state are quantitatively different, which could be measured by the augmentation algorithm. Defects corresponding to reversible rearrangements may even differ from defects corresponding to irreversible rearrangement.

In 2014, Charbonneau, Kurchan, *et al.* [110–112] exactly solved the replica symmetry breaking solution for the distribution of contact forces

$$P(f) \sim f^\theta, \quad (4.1)$$

and showed that their solution held for the infinite dimensional case with $\theta = 0.42311$. However, they found that this prediction became less accurate at low dimensions. They went on to demonstrate that this could be resolved and the mean-field value recovered. By splitting the distribution into a localized and an extended part, they create two distinct power laws. They found that buckling particles, described as particles with exactly $d + 1$ contact, had an exponent of $\theta_l = 0.17462$, while the exponent for the rest-labeled extended modes, has an exponent of $\theta_e = 0.42311$. The full scaling relation is then

$$P(f) = n_l P_l(f) + (1 - n_l) P_e(f). \quad (4.2)$$

The question then becomes: how do you determine which modes or particles to label as local, and which as extended. The work outlined in this thesis gives insight into this problem. We have also observed two kinds of events—the small network events and the extended rearrangement events. It seems promising that the scaling of network events would follow the localized scaling, and the rearrangement events would follow the extended scaling. Additionally, the defects found in Chapter 2 correspond to rearrangements, and thus the extended modes.

Bibliography

- [1] Andrea J Liu and Sidney R. Nagel. Nonlinear dynamics: Jamming is not just cool any more. *Nature*, 396(6706):21–22, 1998. ISSN 0028-0836. doi: 10.1038/23819. URL http://www.nature.com/nature/journal/v396/n6706/full/396021a0.html\files/790/Liu_Nagel_1998_Nonlineardynamics.pdf.
- [2] Leonardo E. Silbert, Andrea J. Liu, and Sidney R. Nagel. Vibrations and diverging length scales near the unjamming transition. *Physical Review Letters*, 95(9):098301, 8 2005. ISSN 00319007. doi: 10.1103/PhysRevLett.95.098301. URL <http://link.aps.org/doi/10.1103/PhysRevLett.95.098301>.
- [3] Carl F. Schreck, Robert S. Hoy, Mark D. Shattuck, and Corey S. O'Hern. Particle-scale reversibility in athermal particulate media below jamming. *Physical Review E - Statistical, Nonlinear, and Soft Matter Physics*, 88(5):052205, 11 2013. ISSN 15393755. doi: 10.1103/PhysRevE.88.052205. URL <http://link.aps.org/doi/10.1103/PhysRevE.88.052205>.
- [4] Yen Shuo Su, Yu Hsuan Liu, and I. Lin. Correlating structural order with structural rearrangement in dusty plasma liquids: Can structural rearrangement be predicted by static structural information? *Physical Review Letters*, 109(19):195002, 11 2012. ISSN 00319007. doi: 10.1103/PhysRevLett.109.195002. URL <http://link.aps.org/doi/10.1103/PhysRevLett.109.195002>.
- [5] Edan Lerner, Gustavo Düring, and Matthieu Wyart. Low-energy non-linear excitations in sphere packings. *Soft Matter*, 9(34):8252, 8 2013. ISSN 1744-683X. doi: 10.1039/c3sm50515d. URL <http://xlink.rsc.org/?DOI=c3sm50515d>.
- [6] Peter Schall, David A. Weitz, and Frans Spaepen. Structural rearrangements that govern flow in colloidal glasses. *Science*, 318(5858):1895–1899, 12 2007. ISSN

- 1095-9203. doi: 10.1126/science.1149308. URL <http://www.ncbi.nlm.nih.gov/pubmed/18096800>.
- [7] Nathan C. Keim and Paulo E. Arratia. Yielding and microstructure in a 2D jammed material under shear deformation. *Soft Matter*, 9(27):6222, 2013. ISSN 1744-683X. doi: 10.1039/c3sm51014j. URL <http://xlink.rsc.org/?DOI=c3sm51014j>
<http://www.scopus.com/inward/record.url?eid=2-s2.0-84881055679&partnerID=tZ0tx3y1>.
- [8] Julia K. Morgan and Margaret S. Boettcher. Numerical simulations of granular shear zones using the distinct element method: 1. Shear zone kinematics and the micromechanics of localization. *Journal of Geophysical Research*, 104(B2):2703, 1999. ISSN 0148-0227. doi: 10.1029/1998JB900056.
- [9] Merlijn S. van Deen, Johannes Simon, Zorana Zeravcic, Simon Dagois-Bohy, Brian P. Tighe, and Martin van Hecke. Contact changes near jamming. *Physical Review E*, 90(2):020202, 8 2014. ISSN 1539-3755. doi: 10.1103/PhysRevE.90.020202. URL <http://arxiv.org/pdf/1404.3156v1.pdf>
<http://link.aps.org/doi/10.1103/PhysRevE.90.020202>
<http://arxiv.org/abs/1404.3156v1>.
- [10] M. Lisa Manning and Andrea J. Liu. Vibrational modes identify soft spots in a sheared disordered packing. *Physical Review Letters*, 107(10), 2011. ISSN 00319007. doi: 10.1103/PhysRevLett.107.108302. URL <http://prl.aps.org/abstract/PRL/v107/i10/e108302>
<http://journals.aps.org/prl/abstract/10.1103/PhysRevLett.107.108302>.
- [11] Craig E. Maloney and Anal Lemaître. Amorphous systems in athermal, quasistatic shear. *Physical Review E - Statistical, Nonlinear, and Soft Matter Physics*, 74(1):016118, 7 2006. ISSN 15393755. doi: 10.1103/PhysRevE.74.016118. URL <http://www.ncbi.nlm.nih.gov/pubmed/16907162>.
- [12] K. Michael Salerno, Craig E. Maloney, and Mark O. Robbins. Avalanches in strained amorphous solids: Does inertia destroy critical behavior? *Physical Review Letters*, 109(10):105703, 9 2012. ISSN 00319007. doi: 10.1103/PhysRevLett.109.105703. URL <http://link.aps.org/doi/10.1103/PhysRevLett.109.105703>.
- [13] K. Michael Salerno and Mark O. Robbins. Effect of inertia on sheared disordered solids: Critical scaling of avalanches in two and three dimensions. *Physical Review*

- E - Statistical, Nonlinear, and Soft Matter Physics*, 88(6):062206, 12 2013. ISSN 15393755. doi: 10.1103/PhysRevE.88.062206. URL <http://link.aps.org/doi/10.1103/PhysRevE.88.062206>.
- [14] Yunfeng Shi, Michael B. Katz, Hui Li, and Michael L. Falk. Evaluation of the disorder temperature and free-volume formalisms via simulations of shear banding in amorphous solids. *Physical Review Letters*, 98(18):1–4, 2007. ISSN 00319007. doi: 10.1103/PhysRevLett.98.185505.
- [15] M. Lisa Manning, James S. Langer, and J. M. Carlson. Strain localization in a shear transformation zone model for amorphous solids. *Physical Review E - Statistical, Nonlinear, and Soft Matter Physics*, 76(5):056106, 2007. ISSN 15393755. doi: 10.1103/PhysRevE.76.056106. URL <http://pre.aps.org/abstract/PRE/v76/i5/e056106>.
- [16] V Chikkadi, D M Miedema, B Nienhuis, and P Schall. Shear banding of colloidal glasses - a dynamic first order transition? *Physical Review Letters*, 113(20):208301, 11 2014. ISSN 10797114. doi: 10.1103/PhysRevLett.113.208301. URL <http://link.aps.org/doi/10.1103/PhysRevLett.113.208301>.
- [17] Kirsten Martens, Lydric Bocquet, and Jean-Louis Barrat. Spontaneous formation of permanent shear bands in a mesoscopic model of flowing disordered matter. *Soft Matter*, 8(15):4197, 2012. ISSN 1744-683X. doi: 10.1039/c2sm07090a.
- [18] G. I. Taylor. The Mechanism of Plastic Deformation of Crystals. Part I. Theoretical. *Proceedings of the Royal Society A: Mathematical, Physical and Engineering Sciences*, 145(855):362–387, 7 1934. ISSN 1364-5021. doi: 10.1098/rspa.1934.0106. URL <http://rspa.royalsocietypublishing.org/cgi/doi/10.1098/rspa.1934.0106>.
- [19] Steven Slotterback, Mitch Mailman, Krisztian Ronaszegi, Martin Van Hecke, Michelle Girvan, and Wolfgang Losert. Onset of irreversibility in cyclic shear of granular packings. *Physical Review E - Statistical, Nonlinear, and Soft Matter Physics*, 85(2):021309, 2 2012. ISSN 15393755. doi: 10.1103/PhysRevE.85.021309. URL <http://link.aps.org/doi/10.1103/PhysRevE.85.021309>.
- [20] David L. Henann and Ken Kamrin. Continuum Modeling of Secondary Rheology in Dense Granular Materials. *Physical Review Letters*, 113(17):178001, 10 2014. ISSN

- 0031-9007. doi: 10.1103/PhysRevLett.113.178001. URL <http://link.aps.org/doi/10.1103/PhysRevLett.113.178001>.
- [21] C Coulais, a Seguin, and O Dauchot. Shear modulus and Dilatancy Softening in Granular Packings above Jamming. *Physical Review Letters*, 113(19):1–5, 11 2014. ISSN 10797114. doi: 10.1103/PhysRevLett.113.198001. URL <http://link.aps.org/doi/10.1103/PhysRevLett.113.198001>.
- [22] Michael L. Falk and James S. Langer. Dynamics of Viscoplastic Deformation in Amorphous Solids. *Physical Review E*, 57(6):16, 6 1997. ISSN 1063-651X. doi: 10.1103/PhysRevE.57.7192. URL <http://arxiv.org/abs/cond-mat/9712114>.
- [23] Davide Fiocco, Giuseppe Foffi, and Srikanth Sastry. Encoding of memory in sheared amorphous solids. *Physical Review Letters*, 112(2):025702, 1 2014. ISSN 00319007. doi: 10.1103/PhysRevLett.112.025702. URL <http://link.aps.org/doi/10.1103/PhysRevLett.112.025702>.
- [24] Michael L. Falk and James S. Langer. Deformation and Failure of Amorphous Solidlike Materials. *Annual Review of Condensed Matter Physics*, 2(1):28, 3 2010. ISSN 1947-5454. doi: 10.1146/annurev-conmatphys-062910-140452. URL <http://arxiv.org/abs/1004.4684>.
- [25] Peter Sollich, Francois Lequeux, Pascal Hebraud, and Michael E Cates. Rheology of Soft Glassy Materials. *Physical Review Letters*, 78(10):4, 3 1996. ISSN 0295-5075. doi: 10.1103/PhysRevLett.78.2020. URL <http://arxiv.org/abs/cond-mat/9611228>.
- [26] Peter Sollich. Rheological constitutive equation for model of soft glassy materials. *Physical Review E*, 58(1):24, 7 1997. ISSN 1063-651X. doi: 10.1103/PhysRevE.58.738. URL <http://arxiv.org/abs/cond-mat/9712001>.
- [27] P. M. Derlet and R. Maaß. Thermal-activation model for freezing and the elastic robustness of bulk metallic glasses. *Physical Review B - Condensed Matter and Materials Physics*, 84(22):2–5, 2011. ISSN 10980121. doi: 10.1103/PhysRevB.84.220201.
- [28] Jean-Christophe Baret, Damien Vandembroucq, and Stphane Roux. Extremal model for amorphous media plasticity. *Physical review letters*, 89(19):195506, 2002. ISSN 0031-9007. doi: 10.1103/PhysRevLett.89.195506.

- [29] Markus Müller and Matthieu Wyart. Marginal Stability in Structural, Spin and Electron Glasses. *Annual Review of Condensed Matter Physics*, 6(1):177–200, 3 2015. ISSN 1947-5454. doi: 10.1146/annurev-conmatphys-031214-014614. URL <http://arxiv.org/pdf/1406.7669.pdf><http://arxiv.org/abs/1406.7669>.
- [30] Joseph D. Paulsen, Nathan C. Keim, and Sidney R. Nagel. Multiple transient memories in experiments on sheared non-brownian suspensions. *Physical Review Letters*, 113(6):068301, 4 2014. ISSN 10797114. doi: 10.1103/PhysRevLett.113.068301. URL <http://link.aps.org/doi/10.1103/PhysRevLett.113.068301><http://arxiv.org/abs/1404.4117>.
- [31] Dapeng Bi, Jie Zhang, Bulbul Chakraborty, and R. P. Behringer. Jamming by shear. *Nature*, 480(7377):355–358, 2011. ISSN 0028-0836. doi: 10.1038/nature10667. URL <http://dx.doi.org/10.1038/nature10667>.
- [32] V Trappe, V Prasad, L Cipelletti, P N Segre, and D a Weitz. Jamming phase diagram for attractive particles. *Nature*, 411(6839):772–775, 2001. ISSN 00280836. doi: 10.1038/35081021.
- [33] Massimo Pica Ciamarra, Raffaele Pastore, Mario Nicodemi, and Antonio Coniglio. Jamming phase diagram for frictional particles. *Physical Review E - Statistical, Nonlinear, and Soft Matter Physics*, 84(4), 2011. ISSN 15393755. doi: 10.1103/PhysRevE.84.041308.
- [34] Thomas K. Haxton, Michael Schmiedeberg, and Andrea J. Liu. Universal Jamming Phase Diagram in the Hard-Sphere Limit. 19104(1):1–8, 2010. doi: 10.1103/PhysRevE.83.031503. URL <http://arxiv.org/abs/1012.0064><http://dx.doi.org/10.1103/PhysRevE.83.031503>.
- [35] Walter Kob and Hans C. Andersen. Testing mode-coupling theory for a supercooled binary Lennard-Jones mixture I: The van Hove correlation function. *Physical Review E*, 51(5):4626–4641, 5 1995. ISSN 1063-651X. doi: 10.1103/PhysRevE.51.4626. URL <https://link.aps.org/doi/10.1103/PhysRevE.51.4626>.
- [36] E. DeGiuli, Edan Lerner, C. Brito, and Matthieu Wyart. The distribution of forces affects vibrational properties in hard sphere glasses. *arXiv*, 2(1):1–8, 2 2014. ISSN 10916490. doi: 10.1073/pnas.1415298111/-/DCSupplemental. URL <http://arxiv.org/abs/1402.3834>.

- [37] Corey S. O'Hern, Leonardo E. Silbert, and Sidney R. Nagel. Jamming at zero temperature and zero applied stress: The epitome of disorder. *Physical Review E*, 68(1):11306, 7 2003. ISSN 1539-3755. doi: 10.1103/PhysRevE.68.011306. URL <http://link.aps.org/doi/10.1103/PhysRevE.68.011306>.
- [38] Daniel M. Sussman, Carl P. Goodrich, Andrea J. Liu, and Sidney R. Nagel. Disordered surface vibrations in jammed sphere packings. *Soft Matter*, 11(14): 2745–2751, 12 2015. ISSN 1744-683X. doi: 10.1039/C4SM02905D. URL <http://arxiv.org/abs/1412.8755><http://xlink.rsc.org/?DOI=C4SM02905D>.
- [39] Silke Henkes, Carolina Brito, and Olivier Dauchot. Extracting vibrational modes from fluctuations: a pedagogical discussion. *Soft Matter*, 8(22):6092, 5 2012. ISSN 1744-683X. doi: 10.1039/c2sm07445a. URL <http://pubs.rsc.org/en/content/articlehtml/2012/sm/c2sm07445a>.
- [40] James S. Langer and M. Lisa Manning. Steady-state, effective-temperature dynamics in a glassy material. *Physical Review E - Statistical, Nonlinear, and Soft Matter Physics*, 76(5):1–9, 2007. ISSN 15393755. doi: 10.1103/PhysRevE.76.056107.
- [41] James S. Langer. Shear-transformation-zone theory of plastic deformation near the glass transition. *Physical Review E - Statistical, Nonlinear, and Soft Matter Physics*, 77(2):1–14, 2008. ISSN 15393755. doi: 10.1103/PhysRevE.77.021502.
- [42] James S. Langer. Shear-transformation-zone theory of yielding in athermal amorphous materials. *Physical Review E*, 92(1):012318, 7 2015. ISSN 1539-3755. doi: 10.1103/PhysRevE.92.012318. URL <http://link.aps.org/doi/10.1103/PhysRevE.92.012318>.
- [43] Jean-philippe Bouchaud. Weak ergodicity breaking and aging in disordered systems. *Journal de Physique I*, 2:1705–1713, 1992. ISSN 1155-4304. doi: 10.1051/jp1:1992238.
- [44] S. M. Fielding, M. E. Cates, and P. Sollich. Shear banding, aging and noise dynamics in soft glassy materials. *Soft Matter*, 5(12): 2378–2382, 2009. ISSN 1744-683X. doi: 10.1039/B812394M. URL <http://pubs.rsc.org/en/Content/ArticleHTML/2009/SM/B812394M><http://arxiv.org/abs/0812.3300><http://xlink.rsc.org/?DOI=B812394M>.

- [45] Guangjun Yin and Michael J. Solomon. Soft glassy rheology model applied to stress relaxation of a thermoreversible colloidal gel. *Journal of Rheology*, 52(3):785, 2008. ISSN 01486055. doi: 10.1122/1.2885738. URL <http://scitation.aip.org/content/sor/journal/jor2/52/3/10.1122/1.2885738>.
- [46] tienne Fodor, Cesare Nardini, Michael E Cates, Julien Tailleur, Paolo Visco, and Frdric van Wijland. How far from equilibrium is active matter? page 5, 4 2016. URL <http://arxiv.org/abs/1604.00953>.
- [47] Atsushi Ikeda, Ludovic Berthier, and Peter Sollich. Unified study of glass and jamming rheology in soft particle systems. *Physical Review Letters*, 109(1):1–5, 2012. ISSN 00319007. doi: 10.1103/PhysRevLett.109.018301.
- [48] Gary L. Hunter and Eric R. Weeks. The Physics of the Colloidal Glass Transition. 066501:52, 2011. ISSN 0034-4885. doi: 10.1088/0034-4885/75/6/066501. URL <http://arxiv.org/abs/1106.3581>.
- [49] Frank H. Stillinger. Supercooled liquids, glass transitions, and the Kauzmann paradox. *The Journal of Chemical Physics*, 88(1988):7818, 1988. ISSN 00219606. doi: 10.1063/1.454295. URL <http://scitation.aip.org/content/aip/journal/jcp/88/12/10.1063/1.454295>.
- [50] S.F. Edwards and R.B.S. Oakeshott. Theory of powders. *Physica A: Statistical Mechanics and its Applications*, 157(3):1080–1090, 6 1989. ISSN 03784371. doi: 10.1016/0378-4371(89)90034-4. URL <http://linkinghub.elsevier.com/retrieve/pii/0378437189900344>.
- [51] Dapeng Bi, Xingbo Yang, M. Cristina Marchetti, and M. Lisa Manning. Motility-driven glass and jamming transitions in biological tissues. 9 2015. URL <http://arxiv.org/abs/1509.06578>.
- [52] Eran Bouchbinder, J. S. Langer, and Itamar Procaccia. Athermal Shear-Transformation-Zone Theory of Amorphous Plastic Deformation II: Analysis of Simulated Amorphous Silicon. pages 1–10, 2006. doi: 10.1103/PhysRevE.75.036108. URL <http://arxiv.org/abs/cond-mat/0611026><http://dx.doi.org/10.1103/PhysRevE.75.036108>.

- [53] R. P. Behringer, Dapeng Bi, B. Chakraborty, S. Henkes, and R. R. Hartley. Why do granular materials stiffen with shear rate? Test of novel stress-based statistics. *Physical Review Letters*, 101(26):1–4, 2008. ISSN 00319007. doi: 10.1103/PhysRevLett.101.268301.
- [54] M.I. Smith. Fracture of Jammed Colloidal Suspensions. *Scientific Reports*, 5:14175, 2015. ISSN 2045-2322. doi: 10.1038/srep14175. URL <http://www.nature.com/doifinder/10.1038/srep14175>.
- [55] Dapeng Bi and Bulbul Chakraborty. Rheology of granular materials: dynamics in a stress landscape. *Philosophical transactions. Series A, Mathematical, physical, and engineering sciences*, 367(1909):5073–5090, 2009. ISSN 1364-503X. doi: 10.1098/rsta.2009.0193.
- [56] Awadhesh K. Dubey, H. George E. Hentschel, Itamar Procaccia, and Murari Singh. Statistics of Plastic Events in Post-Yield Strain-Controlled Amorphous Solids. page 7, 4 2016. URL <http://arxiv.org/abs/1604.04088>.
- [57] Zoe Budrikis and Stefano Zapperi. Avalanche localization and crossover scaling in amorphous plasticity. *Physical Review E - Statistical, Nonlinear, and Soft Matter Physics*, 88(6):062403, 12 2013. ISSN 15393755. doi: 10.1103/PhysRevE.88.062403. URL <http://link.aps.org/doi/10.1103/PhysRevE.88.062403>.
- [58] Stefanos Papanikolaou, Felipe Bohn, Rubem L. Sommer, Gianfranco Durin, Stefano Zapperi, and James P. Sethna. Beyond power laws: Universality in the average avalanche shape. *Nature Physics*, 7(4):13, 1 2009. ISSN 1745-2473. doi: 10.1038/nphys1884. URL <http://arxiv.org/abs/0911.2291>.
- [59] Chen Liu, Ezequiel E. Ferrero, Francesco Puosi, Jean Louis Barrat, and Kirsten Martens. Driving rate dependence of avalanche statistics and shapes at the yielding transition. *Physical Review Letters*, 116(6):1–5, 6 2016. ISSN 10797114. doi: 10.1103/PhysRevLett.116.065501. URL <http://arxiv.org/abs/1506.08161>.
- [60] Mehdi Talamali, Viljo Petäjä, Damien Vandembroucq, and Stphane Roux. Avalanches, precursors, and finite-size fluctuations in a mesoscopic model of amorphous plasticity. *Physical Review E - Statistical, Nonlinear, and Soft Matter Physics*, 84(1):016115, 7 2011. ISSN 15393755. doi: 10.1103/PhysRevE.84.016115. URL <http://link.aps.org/doi/10.1103/PhysRevE.84.016115>.

- [61] Peter Szabo, Peter Dusan Ispanovity, and Istvan Groma. Plastic strain is a mixture of avalanches and quasi-reversible deformations: Study of various sizes. (1):5, 8 2014. ISSN 1550235X. doi: 10.1103/PhysRevB.91.054106. URL <http://arxiv.org/abs/1408.2444>.
- [62] Micah Lundberg, Kapilanjani Krishan, Ning Xu, Corey S. O'Hern, and Michael Dennin. Reversible plastic events in amorphous materials. *Physical Review E - Statistical, Nonlinear, and Soft Matter Physics*, 77(4):041505, 4 2008. ISSN 15393755. doi: 10.1103/PhysRevE.77.041505. URL <http://link.aps.org/doi/10.1103/PhysRevE.77.041505>.
- [63] Nathan C. Keim and Paulo E. Arratia. Mechanical and Microscopic Properties of the Reversible Plastic Regime in a 2D Jammed Material. *Physical Review Letters*, 112(2):028302, 1 2014. ISSN 00319007. doi: 10.1103/PhysRevLett.112.028302. URL <http://link.aps.org/doi/10.1103/PhysRevLett.112.028302>.
- [64] a J Daley, M Rigol, and D S Weiss. Focus on out-of-equilibrium dynamics in strongly interacting one-dimensional systems. *New Journal of Physics*, 16(9):095006, 9 2014. ISSN 1367-2630. doi: 10.1088/1367-2630/16/9/095006. URL <http://stacks.iop.org/1367-2630/16/i=9/a=095006?key=crossref.de4005fc1d7176cae7b6566090508ff4>.
- [65] Patrick Charbonneau, Jorge Kurchan, Giorgio Parisi, Pierfrancesco Urbani, and Francesco Zamponi. Glass and Jamming Transitions: From Exact Results to Finite-Dimensional Descriptions. *Annual Reviews Plant Biology*, 67(February):1–26, 2016. ISSN 1947-5454. doi: 10.1146/)). URL <http://arxiv.org/abs/1406.3533>
<http://arxiv.org/abs/1605.03008>.
- [66] Hajime Yoshino and Francesco Zamponi. Shear modulus of glasses: Results from the full replica-symmetry-breaking solution. *Physical Review E - Statistical, Nonlinear, and Soft Matter Physics*, 90(2):022302, 8 2014. ISSN 15502376. doi: 10.1103/PhysRevE.90.022302. URL <http://link.aps.org/doi/10.1103/PhysRevE.90.022302>.
- [67] Carl P. Goodrich, Simon Dagois-Bohy, Brian P. Tighe, Martin van Hecke, Andrea J. Liu, and Sidney R. Nagel. Jamming in finite systems: stability, anisotropy,

- fluctuations and scaling. *arXiv*, 90(ii):20, 6 2014. ISSN 1539-3755. doi: 10.1103/PhysRevE.90.022138. URL <http://arxiv.org/abs/1406.1529>.
- [68] Ranjan Modak and Subroto Mukerjee. Finite size scaling in crossover among different random matrix ensembles in microscopic lattice models. *arXiv.org*, 16(9):093016, 9 2013. ISSN 13672630. doi: 10.1088/1367-2630/16/9/093016. URL <http://arxiv.org/abs/1310.1443>npapers3://publication/uuid/1CF07DCC-AE9E-41EF-A46E-08383B09112A.
- [69] Carl P. Goodrich, Andrea J. Liu, and Sidney R. Nagel. Finite-size scaling at the jamming transition. *Physical Review Letters*, 109(9):095704, 8 2012. ISSN 00319007. doi: 10.1103/PhysRevLett.109.095704. URL <http://link.aps.org/doi/10.1103/PhysRevLett.109.095704>.
- [70] Asaph Widmer-Cooper, Heidi Perry, Peter Harrowell, and David R. Reichman. Irreversible reorganization in a supercooled liquid originates from localised soft modes. *Nature Physics*, 4(9):711–715, 7 2009. ISSN 1745-2473. doi: 10.1038/nphys1025. URL <http://arxiv.org/abs/0901.3547>.
- [71] a. Tanguy, B. Mantisi, and M. Tsamados. Vibrational modes as a predictor for plasticity in a model glass. *EPL (Europhysics Letters)*, 90(1):16004, 4 2010. ISSN 0295-5075. doi: 10.1209/0295-5075/90/16004. URL <http://stacks.iop.org/0295-5075/90/i=1/a=16004>.
- [72] Samuel S. Schoenholz, Andrea J. Liu, R. a. Riggleman, and J. Rottler. Understanding plastic deformation in thermal glasses from single-soft-spot dynamics. *Physical Review X*, 4(3):031014, 7 2014. ISSN 21603308. doi: 10.1103/PhysRevX.4.031014. URL <http://link.aps.org/doi/10.1103/PhysRevX.4.031014><http://arxiv.org/abs/1404.1403>.
- [73] Jrg Rottler, Samuel S. Schoenholz, and Andrea J. Liu. Predicting plasticity with soft vibrational modes: From dislocations to glasses. *Physical Review E - Statistical, Nonlinear, and Soft Matter Physics*, 89(4):2–6, 2014. ISSN 15502376. doi: 10.1103/PhysRevE.89.042304. URL <http://arxiv.org/abs/1403.0922><http://journals.aps.org/pre/abstract/10.1103/PhysRevE.89.042304>.

- [74] Ekin D. Cubuk, S. S. Schoenholz, J. M. Rieser, B. D. Malone, J. Rottler, D. J. Durian, E. Kaxiras, and Andrea J. Liu. Identifying structural flow defects in disordered solids using machine-learning methods. *Physical Review Letters*, 114(10):108001, 3 2015. ISSN 10797114. doi: 10.1103/PhysRevLett.114.108001. URL <http://link.aps.org/doi/10.1103/PhysRevLett.114.108001>.
- [75] Luka Gartner and Edan Lerner. Nonlinear plastic modes in disordered solids. *Physical Review E*, 93(1):8, 7 2016. ISSN 2470-0045. doi: 10.1103/PhysRevE.93.011001. URL <http://journals.aps.org/pre/abstract/10.1103/PhysRevE.93.011001>.
- [76] Sylvain Patinet, Damien Vandembroucq, and Michael L. Falk. Connecting Local Yield Stresses with Plastic Activity in Amorphous Solids. *Physical Review Letters*, 117(4):045501, 7 2016. ISSN 0031-9007. doi: 10.1103/PhysRevLett.117.045501. URL <http://link.aps.org/doi/10.1103/PhysRevLett.117.045501>.
- [77] Ning Xu, Vincenzo Vitelli, Andrea J. Liu, and Sidney R. Nagel. Anharmonicity and quasi-localization of the excess low-frequency vibrations in jammed solids. *EPL (Europhysics Letters)*, 90(5):6, 6 2009. ISSN 0295-5075. doi: 10.1209/0295-5075/90/56001. URL <http://arxiv.org/abs/0909.3701>.
- [78] Peter Morse, Sven Wijtmans, Merlijn S. van Deen, Martin van Hecke, and M. Lisa Manning. Distinguishing rearrangement events in disordered solids. *In preperation*, pages 2–7, 2017.
- [79] Wen Zheng, Hao Liu, and Ning Xu. Shear-induced solidification of athermal systems with weak attraction. *Physical Review E*, 94(6):062608, 12 2016. ISSN 2470-0045. doi: 10.1103/PhysRevE.94.062608. URL <http://link.aps.org/doi/10.1103/PhysRevE.94.062608>.
- [80] A. W. Lees and S. F. Edwards. The computer study of transport processes under extreme conditions. *Journal of Physics C: Solid State Physics*, 5(15):1921–1928, 8 1972. ISSN 0022-3719. doi: 10.1088/0022-3719/5/15/006. URL <http://stacks.iop.org/0022-3719/5/i=15/a=006?key=crossref.e594e5cd0b6eb0d5dc9f68b23ee836be>.
- [81] <http://www.caam.rice.edu/software/ARPACK/>. URL <http://www.caam.rice.edu/software/ARPACK/>.

- [82] W. v. Muench and H. Statz. *Solid-to-solid diffusion in the gallium arsenide device technology*, volume 9. 1966. ISBN 0030839939. doi: 10.1016/0038-1101(66)90069-4. URL <http://www.amazon.com/Solid-State-Physics-Neil-Ashcroft/dp/0030839939>.
- [83] Carl F. Schreck, Thibault Bertrand, Corey S. O'Hern, and M. D. Shattuck. Repulsive contact interactions make jammed particulate systems inherently non-harmonic. *Physical Review Letters*, 107(7):078301, 8 2011. ISSN 00319007. doi: 10.1103/PhysRevLett.107.078301. URL <http://link.aps.org/doi/10.1103/PhysRevLett.107.078301>.
- [84] Carl P. Goodrich, Andrea J. Liu, and Sidney R. Nagel. Contact nonlinearities and linear response in jammed particulate packings. *Physical Review E*, 90(2):022201, 8 2014. ISSN 1539-3755. doi: 10.1103/PhysRevE.90.022201. URL <http://link.aps.org/doi/10.1103/PhysRevE.90.022201>.
- [85] Claudio Donati, Jack F. Douglas, Walter Kob, Steven J. Plimpton, Peter H. Poole, and Sharon C. Glotzer. Stringlike Cooperative Motion in a Supercooled Liquid. *Physical Review Letters*, 80(11):2338–2341, 3 1998. ISSN 0031-9007. doi: 10.1103/PhysRevLett.80.2338. URL <http://arxiv.org/abs/cond-mat/9706277><http://journals.aps.org/prl/pdf/10.1103/PhysRevLett.80.2338><https://link.aps.org/doi/10.1103/PhysRevLett.80.2338>.
- [86] M. Lisa Manning and Andrea J. Liu. A random matrix definition of the boson peak. *EPL (Europhysics Letters)*, 109(3):36002, 7 2015. ISSN 0295-5075. doi: 10.1209/0295-5075/109/36002. URL <http://stacks.iop.org/0295-5075/109/i=3/a=36002?key=crossref.6feff301ac77239cfed8458d6bc8a278>.
- [87] Amit Shavit, Jack F Douglas, and Robert A Riggleman. Evolution of collective motion in a model glass-forming liquid during physical aging. *The Journal of chemical physics*, 138(12):12A528, 3 2013. ISSN 1089-7690. doi: 10.1063/1.4775781. URL <http://www.pubmedcentral.nih.gov/articlerender.fcgi?artid=3574088&tool=pmcentrez&rendertype=abstract>.
- [88] J. Ding, Sylvain Patinet, Michael L. Falk, Y. Cheng, and E. Ma. Soft spots and their structural signature in a metallic glass. *Proceedings of the National Academy*

- of Sciences*, 111(39):14052–14056, 9 2014. ISSN 0027-8424. doi: 10.1073/pnas.1412095111. URL <http://www.pnas.org/cgi/doi/10.1073/pnas.1412095111>.
- [89] Edan Lerner and Itamar Procaccia. Locality and nonlocality in elastoplastic responses of amorphous solids. *Physical Review E - Statistical, Nonlinear, and Soft Matter Physics*, 79(6):1–10, 2009. ISSN 15393755. doi: 10.1103/PhysRevE.79.066109.
- [90] Thomas B. Schröder, Srikanth Sastry, Jeppe C. Dyre, and Sharon C. Glotzer. Crossover to potential energy landscape dominated dynamics in a model glass-forming liquid. *Journal of Chemical Physics*, 112(22):9834–9840, 2000. ISSN 00219606. doi: 10.1063/1.481621.
- [91] Jorge Nocedal. Updating quasi-Newton matrices with limited storage. *Mathematics of Computation*, 35(151):773–773, 9 1980. ISSN 0025-5718. doi: 10.1090/S0025-5718-1980-0572855-7. URL <http://www.ams.org/mcom/1980-35-151/S0025-5718-1980-0572855-7/>.
- [92] Penghui Cao, Xi Lin, and Harold S. Park. Strain-rate and temperature dependence of yield stress of amorphous solids via self-learning metabasin escape algorithm. *Journal of the Mechanics and Physics of Solids*, 68:239–250, 2014. ISSN 00225096. doi: 10.1016/j.jmps.2014.04.004. URL <http://linkinghub.elsevier.com/retrieve/pii/S0022509614000647>.
- [93] Nathan Perchikov and Eran Bouchbinder. Variable-amplitude oscillatory shear response of amorphous materials. *Physical Review E - Statistical, Nonlinear, and Soft Matter Physics*, 89(6):062307, 6 2014. ISSN 15502376. doi: 10.1103/PhysRevE.89.062307. URL <http://link.aps.org/doi/10.1103/PhysRevE.89.062307>.
- [94] Ke Chen, M. Lisa Manning, Peter J. Yunker, Wouter G. Ellenbroek, Zexin Zhang, Andrea J. Liu, and a. G. Yodh. Measurement of correlations between low-frequency vibrational modes and particle rearrangements in quasi-two-dimensional colloidal glasses. *Physical Review Letters*, 107(10):108301, 8 2011. ISSN 00319007. doi: 10.1103/PhysRevLett.107.108301. URL <http://link.aps.org/doi/10.1103/PhysRevLett.107.108301>.
- [95] Luka Gartner and Edan Lerner. Nonlinear modes disentangle glassy and Goldstone modes in structural glasses. 10 2016. URL <http://arxiv.org/abs/1610.03410>.

- [96] Ekin D. Cubuk, Samuel S. Schoenholz, Jennifer M. Rieser, Brad D. Malone, Joerg Rottler, Douglas J. Durian, Efthimios Kaxiras, and Andrea J. Liu. Identifying structural flow defects in disordered solids using machine learning methods. page 4, 9 2014. URL <http://arxiv.org/abs/1409.6820>.
- [97] A rattler is defined as any particle with less than three contacts.
- [98] Ning Xu, V. Vitelli, Andrea J. Liu, and Sidney R. Nagel. Anharmonic and quasi-localized vibrations in jammed solids Modes for mechanical failure. *EPL (Europhysics Letters)*, 90(5):56001, 6 2010. ISSN 0295-5075. doi: 10.1209/0295-5075/90/56001. URL <http://stacks.iop.org/0295-5075/90/i=5/a=56001?key=crossref.1bd050496d72722a608c959d8f7fd962>.
- [99] Ido Regev, Turab Lookman, and Charles Reichhardt. Onset of irreversibility and chaos in amorphous solids under periodic shear. *Physical Review E - Statistical, Nonlinear, and Soft Matter Physics*, 88(6):1–5, 2013. ISSN 15393755. doi: 10.1103/PhysRevE.88.062401.
- [100] Michel Tsamados, Anne Tanguy, Chay Goldenberg, and Jean Louis Barrat. Local elasticity map and plasticity in a model Lennard-Jones glass. *Physical Review E - Statistical, Nonlinear, and Soft Matter Physics*, 80(2):026112, 8 2009. ISSN 15393755. doi: 10.1103/PhysRevE.80.026112. URL <http://link.aps.org/doi/10.1103/PhysRevE.80.026112>.
- [101] Daniel Vågberg, Peter Olsson, and S Teitel. Universality of Jamming Criticality in Overdamped Shear-Driven Frictionless Disks. *arXiv*, 113(1):5, 12 2013. ISSN 10797114. doi: 10.1103/PhysRevLett.113.148002. URL <http://arxiv.org/abs/1312.5158>.
- [102] Simon Dagois-Bohy, Brian P. Tighe, Johannes Simon, Silke Henkes, and Martin Van Hecke. Soft-sphere packings at finite pressure but unstable to shear. *Physical Review Letters*, 109(9):1–5, 2012. ISSN 00319007. doi: 10.1103/PhysRevLett.109.095703.
- [103] Denis J Evans and Gary P Morriss. *Statistical Mechanics of Nonequilibrium Liquids*. Number 1. 1990. ISBN 9780511535307. doi: 10.1017/CBO9780511535307. URL http://ebooks.cambridge.org/ref/id/CBO9780511535307http://press.anu.edu.au/titles/sm_citation/.

- [104] R J Bell, P Dean, and D C Hibbins-Butler. Localization of normal modes in vitreous silica, germania and beryllium fluoride. *Journal of Physics C: Solid State Physics*, 3 (10):2111–2118, 10 1970. ISSN 0022-3719. doi: 10.1088/0022-3719/3/10/013. URL <http://iopscience.iop.org/article/10.1088/0022-3719/3/10/013>.
- [105] Linge Bai and David Breen. Calculating Center of Mass in an Unbounded 2D Environment, 1 2008. ISSN 2151-237X. URL <http://www.tandfonline.com/doi/abs/10.1080/2151237X.2008.10129266#preview>.
- [106] Matthieu Wyart, Leonardo E. Silbert, Sidney R. Nagel, and Thomas a. Witten. Effects of compression on the vibrational modes of marginally jammed solids. *Physical Review E - Statistical, Nonlinear, and Soft Matter Physics*, 72 (5):051306, 11 2005. ISSN 15393755. doi: 10.1103/PhysRevE.72.051306. URL <http://link.aps.org/doi/10.1103/PhysRevE.72.051306>.
- [107] Vladimir Dailidonis, Valery Ilyin, Pankaj Mishra, and Itamar Procaccia. Consequences of Disorder on the Stability of Amorphous Solids. page 8, 7 2015. URL <http://arxiv.org/abs/1507.01207>.
- [108] Oleg Gendelman, Yoav G. Pollack, Itamar Procaccia, Shiladitya Sengupta, and Jacques Zylberg. What determines force chains in granular media? 5 2015. URL <http://arxiv.org/abs/1505.06626>.
- [109] Oleg Gendelman, Prabhat K. Jaiswal, Itamar Procaccia, Bhaskar Sen Gupta, and Jacques Zylberg. Shear Transformation Zones: State Determined or Protocol Dependent? page 4, 8 2014. ISSN 12864854. doi: 10.1209/0295-5075/109/16002. URL <http://arxiv.org/abs/1408.4139>.
- [110] Jorge Kurchan, Giorgio Parisi, and Francesco Zamponi. Exact theory of dense amorphous hard spheres in high dimension I. The free energy. *Journal of Statistical Mechanics: Theory and Experiment*, 2012(10):P10012, 10 2012. ISSN 1742-5468. doi: 10.1088/1742-5468/2012/10/P10012. URL <http://stacks.iop.org/1742-5468/2012/i=10/a=P10012?key=crossref.4053fa75211fa541262f33974e075cf5>.
- [111] Jorge Kurchan, Giorgio Parisi, Pierfrancesco Urbani, and Francesco Zamponi. Exact theory of dense amorphous hard spheres in high dimension. II. the high density

- regime and the gardner transition. *Journal of Physical Chemistry B*, 117(42):12979–12994, 10 2013. ISSN 15206106. doi: 10.1021/jp402235d. URL <http://arxiv.org/abs/1310.2549><http://pubs.acs.org/doi/abs/10.1021/jp402235d>.
- [112] Patrick Charbonneau, Jorge Kurchan, Giorgio Parisi, Pierfrancesco Urbani, and Francesco Zamponi. Exact theory of dense amorphous hard spheres in high dimension. III. The full replica symmetry breaking solution. *Journal of Statistical Mechanics: Theory and Experiment*, 2014(10):P10009, 10 2014. ISSN 1742-5468. doi: 10.1088/1742-5468/2014/10/P10009. URL <http://stacks.iop.org/1742-5468/2014/i=10/a=P10009?key=crossref.93ca485b5c8a929d2fce0ccc59863568>.

Biographical Data

NAME OF AUTHOR: Sven Frederik Wijtmans

PLACE OF BIRTH: Des Moines, Iowa

DATE OF BIRTH: August 9, 1989

EMAIL: sfwijtma@syr.edu

WEBPAGE: <https://sfwijtma.expressions.syr.edu/>

DEGREES AWARDED:

High School diploma, 2011

Norfolk Academy, Norfolk VA

Bachelor in Physics, 2011

Harvey Mudd College, Claremont CA

CONTRIBUTED TALKS:

APS March Meeting 2013 Identifying Defects in Disordered and Ordered Solids
(Session Y30: Jamming & Shearing)

APS March Meeting 2014 A New Method for Identifying Defects in Disordered
Solids (Session Q18: Disordered and Glassy Systems I)

APS March Meeting 2015 Energy Barriers for Defects in Disordered Solids (Session
L49: Focus Session: Mechanics of Defects and Discontinuities)

ACS Colloid and Surface Science Symposium 2014 A new method for identifying
defects in disordered solids (Glasses/Jamming 7: Order and Disorder)